Demonstration of Passive Acoustic Detection and Tracking of Unmanned Underwater Vehicles

by

Kristen Elizabeth Railey

S.B. Mechanical Engineering, Massachusetts Institute of Technology (2013)

Submitted to the Department of Mechanical Engineering
in partial fulfillment of the requirements for the degree of

Master of Science in Mechanical Engineering

at the

MASSACHUSETTS INSTITUTE OF TECHNOLOGY

and the

WOODS HOLE OCEANOGRAPHIC INSTITUTION

June 2018

Author .....
Department of Mechanical Engineering
May 23, 2018

Certified by .....
Henrik Schmidt
Professor of Mechanical and Ocean Engineering
Massachusetts Institute of Technology
Thesis Supervisor

Certified by .....
Dino Dibiaso
Senior Project Leader
The Charles Stark Draper Laboratory, Inc.
Thesis Supervisor

Accepted by .....
Rohan Abeyaratne
Chairman, Department Committee on Graduate Theses
Massachusetts Institute of Technology

Accepted by .....
Henrik Schmidt
Chairman, Joint Committee for Applied Ocean Science & Engineering
Massachusetts Institute of Technology
Woods Hole Oceanographic Institution

Demonstration of Passive Acoustic Detection and Tracking of Unmanned Underwater Vehicles

by

Kristen Elizabeth Railey

Submitted to the Department of Mechanical Engineering
on May 23, 2018, in partial fulfillment of the
requirements for the degree of
Master of Science in Mechanical Engineering

Abstract

In terms of national security, the advancement of unmanned underwater vehicle (UUV) technology has transformed UUVs from tools for intelligence, surveillance, and reconnaissance and mine countermeasures to autonomous platforms that can perform complex tasks like tracking submarines, jamming, and smart mining. Today, they play a major role in asymmetric warfare, as UUVs have attributes that are desirable for less-established navies. They are covert, easy to deploy, low-cost, and low-risk to personnel. The concern of protecting against UUVs of malicious intent is that existing defense systems fall short in detecting, tracking, and preventing the vehicles from causing harm. Addressing this gap in technology, this thesis is the first to demonstrate passively detecting and tracking UUVs in realistic environments strictly from the vehicle's self-generated noise. This work contributes the first power spectral density estimate of an underway micro-UUV, field experiments in a pond and river detecting a UUV with energy thresholding and spectral filters, and field experiments in a pond and river tracking a UUV using conventional and adaptive beamforming. The spectral filters resulted in a probability of detection of 96 % and false alarms of 18 % at a distance of 100 m, with boat traffic in a river environment. Tracking the vehicle with adaptive beamforming resulted in a $6.2 \pm 5.7^\circ$ absolute difference in bearing. The principal achievement of this work is to quantify how well a UUV can be covertly tracked with knowledge of its spectral features. This work can be implemented into existing passive acoustic surveillance systems and be applied to larger classes of UUVs, which potentially have louder identifying acoustic signatures.

Thesis Supervisor: Henrik Schmidt
Title: Professor of Mechanical and Ocean Engineering
Massachusetts Institute of Technology

Thesis Supervisor: Dino Dibiaso
Title: Senior Project Leader
The Charles Stark Draper Laboratory, Inc.

Acknowledgments

Most of all, I would like to thank Henrik Schmidt for his support of me as a researcher and student. Thank you for all your advice on my thesis and coursework. Also thank you for advocating for me and believing in me as a researcher.

I would also like to thank my co-supervisor, Dino DiBiaso, for his support and guidance – not only on my thesis research but also for my experience at Draper Labs. Thank you for all your feedback and encouragement.

Next I would like to thank all of my colleagues in the Laboratory of Autonomous Marine Sensing Systems – especially Mike Benjamin, Misha Novitzky, Caileigh Fitzgerald, Paul Robinette, Eeshan Bhatt, Rui Chen, Oscar Viquez, Nick Rypkema, Greg Nannig, and Erin Fischell. Thank you for your support, guidance, and friendship.

I'd also like to recognize Joe Edwards, Nick Pulsone, and Doug Hart for their mentorship while at MIT as an undergrad and at MIT Lincoln Laboratory. You inspired me to pursue my master's degree in mechanical engineering, specializing in ocean robotics.

Finally I want to thank my friends and family, especially my parents – Cheryl and Malcolm – and my brothers – Owen and Stuart – for always being there for me. I could not have accomplished this without you. And thank you to Derek, for being my best friend and support system.

To make this research possible, I am grateful for the support from the National Defense Science and Engineering Graduate Fellowship and Draper Labs Fellowship, as well as DARPA for the support of the Bluefin Sandshark unmanned underwater vehicle.

This research was conducted with Government support under and awarded by DoD, Air Force Office of Scientific Research, National Defense Science and Engineering Graduate (NDSEG) Fellowship, 32 CFR 168a.

Contents

1 Introduction **19**

2 Background **23**

2.1 Current State of Technology and Vulnerabilities in UUVs 23

2.1.1 Hull and Propulsion Design 24

2.1.2 Stability 25

2.1.3 Energy 26

2.1.4 Autonomy 27

2.1.5 Communication 28

2.1.6 Sensors 29

2.1.7 Navigation 30

2.2 Applications of UUVs 31

2.2.1 Current Missions 32

2.2.2 Future Missions 32

2.3 Motivation for Detecting and Tracking UUVs 33

2.3.1 U.S. Navy 34

2.3.2 DARPA 34

2.3.3 Rapid Reaction Technology Office 35

2.3.4 Defense Science Board 35

3 Related Work **37**

3.1 Acoustic Spectrum Analysis of UUVs 37

3.2 Automatic Target Recognition 38

3.2.1 Detection with Active Sonar 39

3.2.2 Detection with Passive Sonar 39

3.3 Passive Acoustic Tracking . . . 40

4 Detection and Tracking Theory 43

4.1 Detection Threshold Theory . . . 43

4.1.1 Passive Sonar Equation . . . 43

4.1.2 Receiver Operating Characteristic Curves . . . 44

4.2 Power Spectral Density . . . 45

4.3 Underway Vehicle Detection . . . 46

4.3.1 Short-Time Fourier Transform . . . 46

4.3.2 Energy Calculation . . . 46

4.3.3 Spectral Filters . . . 47

4.3.4 Summary . . . 48

4.4 Beamforming . . . 49

4.4.1 Uniform Linear Arrays . . . 49

4.4.2 Weighted Linear Arrays . . . 54

4.4.3 Array Steering . . . 55

4.4.4 Beamforming on a Moving Target . . . 57

4.4.5 Minimum Power Distortionless Response (MPDR) Beamformer . . . 58

5 Experimental Methods 61

5.1 Bluefin Sandshark UUV . . . 61

5.1.1 Tetrahedral Array . . . 62

5.1.2 Autonomy – MOOS-IvP . . . 63

5.2 Horizontal Line Array . . . 64

5.3 Power Spectral Density Estimate – Test Setup . . . 64

5.4 Jenkins Pond Demonstration – Test Setup . . . 65

5.5 Charles River Demonstration – Test Setup . . . 67

6 Field Experiments and Results 73

6.1 Power Spectral Density Estimate – Results . . . 73

6.2 Jenkins Pond Demonstration – Results . . . 75

6.2.1 Detection . . . 75

6.2.2 Tracking . . . 76

6.3 Charles River Demonstration – Results 80
6.3.1 Detection 81
6.3.2 Tracking 84

7 Conclusion **89**

List of Figures

2-1 Bluefin Robotics line of UUVs: Bluefin Robotics, a major manufacturer of UUVs, produces a range of UUVs that vary by depth rating, which relates to the size of the vehicle. The Hovering AUV (HAUV) is the only vehicle they manufacturer that does not have a torpedo-shaped hull and single propeller design [1]. 25

4-1 Windowing effect on incoming signal $x(t)$: when a window function, $w(t)$, is applied to the signal, the signal becomes segmented, which is used for short-time Fourier transform [55]. 47

4-2 Frequency response of ideal low pass filter: frequencies that are passed through are between positive and negative w, frequencies that are eliminated are represented by the stop-band [78]. 47

4-3 Process for producing ROC curves on a moving target: incoming data from a hydrophone element is analyzed by applying short-time Fourier transform, spectral filtering, and energy thresholding. The result is compared to the true presence of the UUV to calculate probabilities of false alarms and true detections. 49

4-4 Coordinate system for beamforming: elevation and azimuth are defined as θ and ϕ respectively. 50

4-5 Coordinates and element spacing of a line array: a vertical line array measures direction of arrival in elevation, or θ. The elements, which are identified by numbers 0 to N are evenly spaced by Δz [94]. 50

4-6 Filtering process of an array in visual form: the incoming signal on each element of the array $f(t, p_n)$ is filtered by $h_n(\tau)$ and summed together to produce the array output $y(t)$ [94]. 51

4-7 Delay and sum beamforming process in visual form: the signal on each element of the array, $f(t-\tau_n)$, is filtered by applying a delay, $h_n(\tau)$, and summed together to produce the array output $y(t)$ [94]. 53

4-8 Weights for a narrowband beamformer: gain and phase can be modified to create an optimal beamformer [94]. 53

4-9 Comparison of Kaiser and uniform weights: the tradeoff between Kaiser and uniform weights is side lobe height and beamwidth. Kaiser weighting decreases side lobe heights but widens the beamwidth [94]. 55

4-10 Theoretical beampatterns of Charles River array configuration: in each subplot, uniform (blue) and Kaiser (red) weightings are compared. The top figures are beampatterns at 10,000 Hz, the cutoff frequency for spatial aliasing in this configuration. The bottom figures are beampatterns at 5,000 Hz, half of the cutoff frequency for spatial aliasing. The left plots are steered to broadside or 90^o, the right plots are steered to 135^o. 56

4-11 Theoretical beampatterns of Jenkins Pond array configuration: in each subplot, uniform (blue) and Kaiser (red) weightings are compared. The top figures are beampatterns at 3,000 Hz, the cutoff frequency for spatial aliasing in this configuration. The bottom figures are beampatterns at 1,500 Hz, half of the cutoff frequency for spatial aliasing. The left plots are steered to broadside or 90^o, the right plots are steered to 135^o. 57

4-12 Beamforming process for a moving target: to estimate bearing of a moving target, the incoming signal on each array element is segmented into time snapshots, discrete Fourier transform is applied, and frequencies are individually beamformed. The beamformer results across all frequencies are averaged, resulting in a beamformer output over time. 58

5-1 Bluefin Sandshark micro-UUV: this micro-UUV manufactured by Bluefin Robotics was used to demonstrate passive detection and tracking in a pond and river experiment [73]. 61

5-2 Tetrahedral array in nose payload section of the Bluefin Sandshark micro-UUV. 63

5-3 Element configuration of a tetrahedral array: a tetrahedral array is in the nose payload section of the micro-UUV, which was used to collect acoustic data for the PSD estimate of the vehicle. 63

5-4 Hydrophone element HTI-96-MIN: this hydrophone was used to measure the power spectral density estimate of the micro-UUV. Four of the hydrophones are configured in a tetrahedral array in the nose of the Bluefin Sandshark micro-UUV used in these experiments [6]. 64

5-5 Autonomy decision-making process of MOOS-IvP software: MOOS-IvP is configured such that the vehicle computer is separate from the autonomy payload [5]. 64

5-6 Diagram of the horizontal line array and data acquisition setup: data from the horizontal line array was collected using an analog to digital converter, data storage unit, GPS trigger, and power. 65

5-7 Power spectral density estimate experiment at the MIT alumni pool: the Bluefin Sandshark micro-UUV was secured while its propellor revolved at approximately 1.5 m/s. The onboard acoustic sensors collected acoustic noise data. 66

5-8 Satellite image of Jenkins Pond: array was bottom mounted about 10 m off shore and the vehicle followed a loiter behavior about 100 m off shore. 67

5-9 Shore launch of vehicle at Jenkins pond: the UUV was launched from the shore and the array was bottom mounted about 10 m from the shoreline. . . . 68

5-10 UUV track in X-Y coordinates over time at the Jenkins Pond experiment: UUV performed a loiter pattern about 100 m offshore. The progression of time is represented by the colorbar and the total mission time was about 20 min. Navigation data was taken from the vehicle's inertial navigation system. 68

5-11 UUV depth over time at the Jenkins Pond experiment: depth data was taken from vehicle's inertial navigation system. The short periods of zero-depth are the vehicle surfacing for a GPS fix. 69

5-12 UUV speed over time at the Jenkins Pond experiment: speed data was taken from vehicle's inertial navigation system. The short periods of zero-speed are the vehicle surfacing for a GPS fix. 69

5-13 Satellite image of the Charles River: the horizontal line array was mounted on the MIT Sailing Pavilion dock and the vehicle followed a loiter behavior about 100 m off shore. 70

5-14 UUV was launched from the MIT Sailing Pavilion dock at the Charles River and the array was mounted to the dock. 70

5-15 UUV track in X-Y coordinates over time at the Charles River experiment: UUV performed a loiter pattern about 100 m offshore. The progression of time is represented by the colorbar and the total mission time was about 20 min. Navigation data was taken from the vehicle's inertial navigation system. . . . 71

5-16 UUV depth over time at the Charles River experiment: depth data was taken from vehicle's inertial navigation system. The short periods of zero-depth are the vehicle surfacing for a GPS fix. 72

5-17 UUV speed over time at the Charles River experiment: speed data was taken from vehicle's inertial navigation system. The short periods of zero-speed are the vehicle surfacing for a GPS fix. 72

6-1 Spectrogram of the power spectral density estimate experiment at the MIT alumni pool: the spectrogram shows how frequencies change over time in a visual representation. The vehicle exhibited strong frequencies between 16 kHz and 18 kHz. 73

6-2 Power spectral density estimate of Bluefin Sandshark micro-UUV: the power spectral density estimate was derived from acoustic data collected on-board the vehicle. The data was collected in a pool environment. The standard deviation of the data was used as the error margin. 74

6-3 Spectrogram of the Jenkins Pond experiment: the spectrogram shows how frequencies change over time in a visual representation. The vehicle is identifiable by its strong frequency tone at 800 Hz, which is aliased down from the true frequency of 20 kHz. The vehicle enters the water at around 800 s. . . . 76

6-4 ROC curves from the Jenkins Pond experiment: the bandpass filter applied to the aliased frequency of 800 Hz outperforms no filter applied to the data. . 77

6-5 Area under the ROC curves of the Jenkins Pond experiment: the area under the curve is a measure of the ROC curve performance. The bandpass filter increases the area under the curve by about 10 %. 78

6-6 Conventional beamforming results of the Jenkins Pond experiment: the true vehicle track is the triangular pattern shown in the beamformer. There is a broadband interferer at 90 °. 78

6-7 Estimated versus expected bearing of the UUV at the Jenkins Pond experiment with conventional beamforming. 79

6-8 Absolute difference, or error, between the estimated and expected bearing of the vehicle over time at the Jenkins Pond experiment with conventional beamforming 80

6-9 MPDR beamforming results of Jenkins Pond experiment: the vehicle true vehicle track is the triangular pattern shown in the beamformer. There is a broadband interferer at 90 °. 80

6-10 Estimated versus expected bearing of the UUV at the Jenkins Pond experiment with MPDR beamforming. 81

6-11 Absolute difference, or error, between the estimated and expected bearing of the vehicle over time at the Jenkins Pond experiment with MPDR beamforming. 82

6-12 Spectrogram of the Charles River experiment: the spectrogram shows how frequencies change over time in a visual representation. The vehicle is identifiable by its strong frequency tone at 17500 Hz, which is aliased down from the true frequency of 20 kHz. The vehicle enters the water at around 300 s. . . 82

6-13 ROC curves from the Charles River experiment: three different filters were applied to the dataset to increase the SNR of the vehicle signature. The first filter was a bandpass filter from 16 kHz to 18 kHz. The second filter was the PSD estimate as a frequency shaping filter. Finally, the third filter was a combination of the bandpass filter and the PSD filter. The combination of the bandpass filter and PSD filter outperformed the other spectral filters. No filter applied, represented in red, performed the worst. 83

6-14 Area under the ROC curves of the Charles River experiment: the area under the curve is a measure of the ROC curve performance. The PSD and bandpass filter combination increases the area under the curve by about 10% from no filter applied 84
6-15 Conventional beamforming results of the Charles River experiment: the true vehicle track is the triangular pattern shown in the beamformer. 85
6-16 Estimated versus expected bearing of the UUV at the Charles River experiment with conventional beamforming. 85
6-17 Absolute difference, or error, between the estimated and expected bearing of the vehicle over time at the Charles River experiment with conventional beamforming 86
6-18 MPDR beamforming results of Charles River experiment: the true vehicle track is the triangular pattern shown in the beamformer. 86
6-19 Estimated versus expected bearing of the UUV at the Charles River experiment with MPDR beamforming. 87
6-20 Absolute difference, or error, between the estimated and expected bearing of the vehicle over time at the Charles River experiment with MPDR beamforming. 87

List of Tables

2.1 Summary of UUV size classes: UUVs are categorized by their size, which is correlated to endurance and payload size [12]. 24

4.1 Detection algorithm decisions and probability definitions: the result of the detection algorithm will either be a correct detection, false alarm, missed detection, or correct no detection. 44

4.2 Array specifications used in the Jenkins Pond and Charles River experiments: the Jenkins Pond array had a wider aperture than the Charles River array due to the increase in the number of elements and element spacing; however, it had lower cutoff frequency for spatial aliasing. 56

5.1 Bluefin Sandshark micro-UUV dimensions and performance specifications: the micro-UUV is a man-portable platform and a member of the smallest class of UUVs [73]. 62

6.1 Probability of detection and false alarms from the ideal detection threshold for the Jenkins Pond experiment. The bandpass filter was applied to the aliased frequency of 800 Hz. 76

6.2 Comparison of absolute angle difference, or error, between conventional and MPDR beamforming at the Jenkins Pond experiment 79

6.3 Probability of detection and false alarms from the ideal detection threshold for the Charles River experiment. The bandpass and PSD filter combination had the best performance. 83

6.4 Comparison of absolute angle difference, or error, between conventional and MPDR beamforming at the Charles River experiment. 87

Chapter 1

Introduction

Due to their growing technical maturity, unmanned underwater vehicles (UUVs) are now considered valuable assets to multiple industries: defense, oil and gas, environmental monitoring, and salvage. Today, UUVs take on missions that were previously considered impossible with traditional maritime platforms such as ships, divers, and submarines. For example, UUVs are capable of tracking plumes [79], following submarines [36], detecting mines [46], and collecting environmental data under ice [19]– all missions that were once too "dull, dirty, and dangerous" to complete [87].

From advancing technology in sensing, autonomy, and communication, UUVs have overcome some of the most challenging aspects of working in an ocean environment. For instance, improving artificial intelligence has enabled UUVs to perform longer missions without human supervision, such as adapting to the ocean environment to search for submarines [54]. In addition, UUVs have benefited from improved energy storage and small size, weight, and power (SWAP) sensors.

However, with new capabilities come new threats. In terms of national security, UUVs are now useful tools for tracking submarines [57], invading harbors [49], and collecting oceanographic data in restricted areas [13]. They are desirable for their covertness, ability to navigate shallow waters, and multiplication of force. Some classes of UUVs are viewed as disposable assets because of their low cost [61]. To rise to the challenge, the U.S. Department of Defense has published multiple calls for proposals to detect and track UUVs. DARPA requested an "Open Ocean Counter Unmanned Underwater Vehicle (OOCUUV) Study" [30], Strategic Systems Program for Nuclear Weapons Security has called for small business

innovation research (SBIR) for "Unmanned Undersea Vehicle (UUV) Detection and Classification in Harbor Environments" [4], and the U.S. Department of the Navy has requested a "Counter-Unmanned Undersea Vehicle (C-UUV) Capability Demonstration for the Stiletto Maritime Demonstration Program" [2].

The motivation of this thesis stems from the urgent demand for counter-UUV technology. This thesis is the first demonstration of passively detecting and tracking an autonomous underwater vehicle strictly from its self-generated noise. The contributions include:

1. Analysis of the frequency spectrum of a micro-UUV's self-generated noise

2. Field experiments in a pond and river quantifying the detection and false alarm rates of a UUV with different spectral filters

3. Field experiments in a pond and river demonstrating tracking a UUV using conventional and adaptive beamforming on a horizontal line array.

The work from this thesis answers one of the many critical questions to the counter-UUV problem: how well can a UUV be passively detected and tracked using acoustics in a realistic environment?

This thesis begins with an overview of what UUVs are and what they are used for. This general background sets the stage for why counter-UUV technology is important and how it can be accomplished. This thesis demonstrates how the electro-mechanical noise generated by the UUV is a vulnerability – that it can be used to detect and track UUVs with passive acoustics.

The next chapter describes work related to detecting and tracking UUVs with passive sonar. This chapter includes the current studies of UUV's acoustic noise as well as existing passive tracking systems for maritime applications.

Following the background and related work, the fourth chapter, on detection and tracking theory, illustrates the technical concepts and derivations for finding UUVs with passive acoustics.

In the fifth chapter, experimental methods are described, including the array configuration, robot specifications, and test bed descriptions. The sixth chapter is on field experiments and results, summarizing three experiments: power spectral density estimate and two demonstrations of passive detection and tracking.

Finally, the concluding chapter is a synopsis of the relevant results, implications of this work for the field, and next steps.

Chapter 2

Background

2.1 Current State of Technology and Vulnerabilities in UUVs

The purpose of this section is to give a short overview of UUV subsystems to show what electro-mechanical systems could cause acoustic noise, allowing the vehicle to be detected and tracked passively. In addition, this section emphasizes how common the subsystems are to all classes of UUVs. Because they share these subsystems, UUVs will potentially have similar causes of acoustic noise. Consequently, the demonstration of passively detecting and tracking UUVs done with the Bluefin Sandshark micro-UUV in this thesis could be representative of other UUVs, particularly UUVs optimized for endurance with a single propeller and minimal appendages.

Autonomous underwater vehicles are defined as being unmanned, untethered, and self-propelled [16] [27]. On-board, they carry actuators, sensors and intelligence to complete missions without guidance of a human operator [16].

UUV design is influenced by application; therefore, UUVs range dramatically in size and speed, as well as in depth rating [16] [27]. For example, UUVs for mine countermeasures operate in shallow waters so they require a depth rating of only 200 m [16] [18]. On the other hand, vehicles for deep-sea surveys for marine geology, such as in the oil and gas industries, have a depth rating of 3000 - 6000 m [16] [99]. A UUV can be between 5 kg and 9000 kg, and have a speed of 0.5 m/s to 5 m/s [16]. Despite these differences, the most common design of

a UUV is a torpedo-shaped hull with a propeller and fins for control [16] [99].

Being autonomous, the vehicle can handle its own dynamic control, such as ballasting, pitch, and roll, as well as its mission control [16]. The vehicle has an onboard computer(s) to handle the decision-making [16]. In some cases, acoustic communication is available so a human operator can provide some guidance such as mission control [16].

The sensors on UUVs vary by mission and can include sonar for bathymetry and conductivity, temperature, and depth (CTD) measurements for water column analysis [16] [99] [47].

In more detail, the UUV subsystems can be broken down into: hull design, propulsion, stability, energy, autonomy, communication, sensors, and navigation.

2.1.1 Hull and Propulsion Design

One approach to dividing up UUVs into classes is based on size and weight: man-portable, lightweight, and heavyweight [97]. Below, Table 2.1, summarizes the different classes of vehicles.

Class	Diameter [in]	Displacement [lbs]	Endurance, High Hotel Load [hours]	Endurance, Low Hotel Load [hours]	Payload [ft^3]
Man-portable	3 - 9	<100	<10	10 - 20	<0.25
Lightweight	12.75	~ 500	10 - 20	20 - 40	1 - 3
Heavyweight	21	$<3{,}000$	20 - 50	40 - 80	4 - 6
Large	>36	$\sim 20{,}000$	100 - 300	>400	15 - 30

Table 2.1: Summary of UUV size classes: UUVs are categorized by their size, which is correlated to endurance and payload size [12].

Across all of these size categories, the hydrodynamics and propulsion systems of UUVs are designed around application. A vehicle optimized for endurance has a streamlined hull, few appendages, and an efficient, single propeller [16]. The propeller is usually driven by a brushless DC current motor for its high efficiency [12]. Vehicles that are designed with station-keeping in mind, not long distances, use many thrusters to maneuver the vehicle vertically and laterally [12].

For the common navy applications of intelligence, surveillance, and reconnaissance, and mine countermeasures, UUVs are designed for long endurance. For example, all vehicles

in the Bluefin Robotics line of UUVs, pictured in Figure 2-1, share this optimized design: minimal appendages, tube-shaped, and single propeller.

Outside of the common torpedo-shaped hull design with single propeller, flapping-fin propulsion has been researched for enabling highly maneuverable underwater vehicles [15]. Reverse engineering fish propulsion is inspired by the fact that swimming animals are adept at maneuvering and sensing an underwater world [15]. Bandyopadhyay gives an overview of mature bio-inspired robots, many of which are from the Naval Undersea Warfare Center.

The electromechanical propulsion system of UUVs is a major source of acoustic noise. The cavitation caused by the propeller creates broadband noise that could be used to not only identify the vehicle, but also track it.

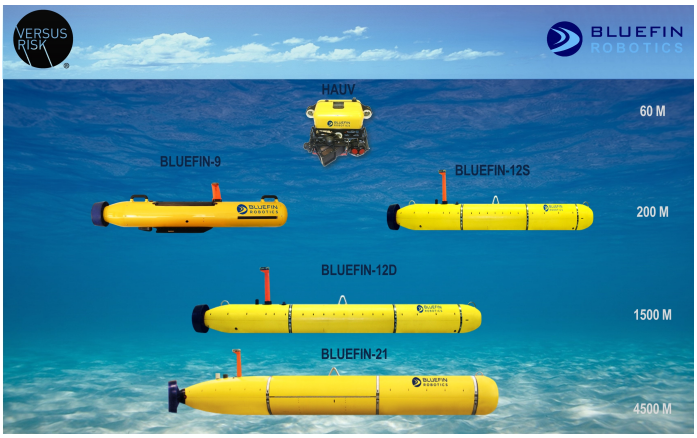

Figure 2-1: Bluefin Robotics line of UUVs: Bluefin Robotics, a major manufacturer of UUVs, produces a range of UUVs that vary by depth rating, which relates to the size of the vehicle. The Hovering AUV (HAUV) is the only vehicle they manufacturer that does not have a torpedo-shaped hull and single propeller design [1].

2.1.2 Stability

Speed and endurance are a trade-off to stability in UUVs [12]. UUVs with fine control for maneuvering have many thrusters to station-keep. Although they can adeptly maneuver, they do not have the endurance of torpedo-shaped, single propeller UUVs [16]. Vehicles without multiple thrusters rely on fins to change the direction of their movements.

The fins and additional thrusters to stabilize and control the vehicle generate unwanted acoustic noise like the propulsion system. This can be used to further identify the vehicle

with passive acoustics.

All UUVs are equipped with a ballast system that is either fixed or variable [12]. Underway, the ballast keeps the UUV neutrally buoyant [12]. During emergencies, the vehicle has a drop weight so it can immediately surface [12]. Stabilizing the UUV on the surface is particularly difficult due to waves, as is having the vehicle dive from the surface [12].

During deployment, UUVs frequently resurface to receive a GPS fix to aid navigation underwater. Due to the difficulty of diving, UUVs will spend an unavoidable, large amount of time on the surface, making them vulnerable to being sighted.

Triantafyllou et al. are a comprehensive review of underwater vehicle maneuvering and control, covering the topics of propellers and propulsion, hydrodynamic forces on the vehicle, and transfer functions and stability [95].

2.1.3 Energy

Due to the limitation of being underwater, autonomous underwater vehicles are battery-powered. The UUV requires power for endurance, speed, and sensors [12]. AUVSI RAND reported that the technology behind propulsion power and energy is the second most challenging aspect of UUV research, behind autonomy [12]. To emphasize the shortcomings of energy in UUVs, a heavyweight vehicle class with a low hotel load has an endurance of only three days [12].

In the 1980s lead-acid batteries were commonly used in UUVs but they have low energy given their weight. The primary energy source found in today's UUVs is lithium ion secondary batteries [75] [58]. Hasvold et al. give a comparison of typical electrochemical power sources in UUVs – comparing aspects like energy density, cost, and rechargeability. For integrating batteries into UUVs, Bradley et al. examine problems with operating at different temperatures, combining individual cells, battery monitoring, and charging and discharging, as well as the trade-offs of power, speed, and range [18].

A future replacement for the energy source in UUVs could be fuel cell power systems [75] [12]. Mendez et al. give an overview of fuel cells for UUVs, which have higher specific energy than batteries.

2.1.4 Autonomy

A definition of decision autonomy is to "sense, interpret and act upon unforeseen changes in the environment and the UUV itself" [56]. According to AUVSI RAND, autonomy is considered to be the greatest long-term challenge of the development of UUVs [12]. Especially for long missions, the UUV needs to be able to sustain itself and recuperate from any malfunctions [56]. This could mean changing its mission, for example re-planning its path if it expects to run out of energy [56].

At a high level, there are two autonomy architectures: sense-plan-act and reactive. Sense-plan-act is one method of the control architecture of the vehicle's sensors and actuators [56]. This system tries to accurately model the environment around it from sensor input and act on the model [56]. Modeling the ocean accurately on a small temporal and spatial scale on-board a UUV is challenging, however. Accurate ocean modeling requires various types of data, lots of computing power, and historical statistics. For example, an ocean modeling system, HYCOM, outputs daily predictions at the Navy DoD Supercomputing Resource Center [7].

On the other hand, reactive control architectures do not plan but rather "react" to the world around them [56]. An autonomy mission example of this would be to transit to a waypoint, gather bathymetric data, and avoid collisions [56]. The resulting action as the vehicle progresses would depend on the environment in the moment [56].

The challenge of working in an ocean environment is that it is constantly changing. It is difficult to model the ocean environment onboard a UUV with precision and accuracy. In addition, defining autonomous behaviors for every possible scenario is a demanding – indeed, impossible – requirement.

Despite the daunting challenge of working in the ocean autonomously, artificial intelligence in UUVs has made great strides. Marine autonomy has evolved past following waypoints for surveying to highly complex missions, including coordinated swarms that can perform optimal time path planning on dynamic ocean flows [69]. *Marine Robot Autonomy* is an up-to-date and extensive overview of autonomy for underwater robots, covering architectures such as MOOS-IvP; limitations to achieving true autonomy like underwater navigation; and specific algorithms, including simultaneous localization and mapping (SLAM) [85].

Coordinating a fleet of autonomous mobile marine platforms is an important area of research, since having multiple robots would make it possible to cover large areas of the ocean over long amounts of time. The advanced autonomy architecture required to control a collaborative network of vehicles goes beyond behavior-based autonomy. Henrik et al. describe how the nested autonomy paradigm, with its core feature of integrated sensing, modeling, and control, is key to multi-vehicle missions [83]. With nested autonomy, each vehicle is capable of detecting, classifying, localizing, and tracking an ocean event of interest, like a subsea volcanic plume [83]. Henrik et al. discuss examples of nested autonomy in field experiments, including adaptive thermocline tracking and bistatic target tracking [83]. These experiments involved up to seven UUVs, equipped with underwater acoustic communication modules [83]. The software was implemented using MOOS-IvP, an open-source behavior-based, autonomous command and control architecture [83].

Other examples of multi-vehicle coordination and advanced autonomy are using cooperative gliders for environmental monitoring discussed in Leonard, and time-optimal path planning for swarms of vehicles that can account for uncertain, three-dimensional, and dynamic flow fields with constraints such as forbidden regions [66] [67]. Ehlers et al. give an overview of the autonomy framework needed for cooperative vehicle target tracking [38].

Another important aspect of autonomy – risk management – is evaluated in Brito et al. Assessment of risk is needed for true autonomy, as vehicles and their stakeholders need to understand the consequences of certain decisions in a dynamic and unstructured environment like the ocean [21]. The authors discuss risk of loss, collision, failure and more [21].

2.1.5 Communication

UUVs have a communication suite that operates differently when the vehicle is underway and on the surface. Above water, UUVs rely on a mast with antennas of electromagnetic sensors to communicate [12]. On the mast, the UUV usually has a configuration of Wi-Fi, GPS, and satellite communication. Underwater, electromagnetic waves attenuate. As a consequence, UUVs predominately use acoustic communication such as the WHOI Micro Modem [88]. A list of acoustic modems with maximum bit rate, range, and frequency band is provided in Stojanovic et al.

Although acoustic modems are commercially available, the acoustic underwater channel

is considered one of the most difficult media to work in because of three properties: attenuation that depends on signal frequency, multi-path propagation, and the limited speed of sound (1500 m/s) [89] [88].

Acoustic propagation requires low frequencies for longer distances which lowers the bandwidth available for communication [12] [89]. The speed of sound also limits communication between UUVs and operators: acoustic communication for 5 km requires approximately 6.7 s round trip [16]. Other concerns of underwater communication include Doppler shifting and spreading caused by motion [89]. In addition, random signal variation is caused by fluctuations in sound speed due to surface waves, turbulence, and other small-scale fluctuations [89]. An overview of the history, applications, propagation channel characteristics, signal processing concepts, and future trends of acoustic communication is covered by Stojanovic et al. [88].

Acoustic communication is a major vulnerability in UUV operations. In situations where covertness is important, using acoustic communication can reveal the presence and location of a UUV. In addition, the low data rates and slow communication times can lead to mission failure when immediate and detailed information is needed by the UUV. For instance, if the vehicle was slow and unresponsive to an abort signal, it could jeopardize the operation.

2.1.6 Sensors

Examples of sensors on UUVs include sonar; magnetic; electromagnetic; optical; chemical, biological, radiological and nuclear defense (CNBRE); and conductivity, temperature and depth (CTD) [12]. The purpose of integrating a suite of sensors on UUVs is not just for interpreting and navigating the unmapped world of the ocean, but also for weather forecasting, oceanographic modeling, mine clearing, and tracking marine life. UUVs have many advantages over research vessels that would normally perform these missions: cost, in-situ environmental analysis at depth, adaptive and event-triggered sampling methods, persistence over long ranges, and minimal human supervision.

Sensors on UUVs can be categorized into acoustic and non-acoustic sensors. For the former, UUVs use sonar both actively and passively. Active sonar is for mapping, detection, and collision avoidance, while passive sonar can be used for anti-submarine warfare. Historically, acoustics have been the main measurement tool for evaluating the spatial-temporal

changes in the ocean [47].

For an overview of non-acoustic sensors, Fries et al. describe chemical instrumentation used on UUVs, including underwater mass spectrometers. To gather information like light absorption, scattering, fluorescence, and radiance, optical instruments have been implemented into UUVs [47]. UUVs are also equipped to measure salinity which is used to characterize seawater, since it is related to density and the solubility of gases. Furthermore, salinity informs oceanographic circulation and mixing [47].

A concern of using passive acoustic sensors onboard a UUV is interference from vehicle self-generated noise. For active sonar, like acoustic communication, it can reveal the location of the vehicle to adversaries. Another trade-off for selecting sensors is the limitation of size, weight, and power (SWAP) onboard the vehicle. For example, the micro-UUV used in this thesis lacks a Doppler velocity logger because of its SWAP constraints.

2.1.7 Navigation

Navigation, as in unmanned aerial and ground vehicles, is critical to UUV missions for several reasons: safety, recovery, and accuracy of the data collected [65]. Mapping and mine clearing are examples of missions that are only effective with accurate and precise location information [65].

UUV navigation is considered challenging because of the lack of GPS [65]. GPS is not available to underwater vehicles because electromagnetic radiation is absorbed in the ocean. Generally, for navy operations, UUVs avoid resurfacing for a GPS fix to avoid being detected. When they do surface, UUVs could be denied GPS due to jamming [81].

To compensate for this, UUV testbeds have acoustic beacons, with known locations, to be a reference to the vehicle [65]. For example, the long base-line system (LBL) has an array of acoustic transponders that cover about $100\,km^2$ [16]. This setup can locate a UUV with an accuracy of several meters [16]. Alternatively, instead of deploying arrays for the LBL system, the transponder can be mounted on a ship [16]. Although acoustic beacon setups improve navigation precision, they reduce the area of operation to the order of squared kilometers and are lots of work to deploy [65].

Without this setup, the UUV would have to use dead reckoning, which relies on data from the vehicle's compass, Doppler velocity logger (DVL), or inertial navigation system [65] [16].

A vehicle is typically equipped with an inertial navigation system (INS) that includes three perpendicular accelerometers and a gyroscope [81]. The acceleration data is integrated to find velocity and position [81]. The measurement results from the combination of sensors are then filtered, such as through a Kalman filter, to estimate and correct for navigation errors [12]. The accuracy of these measurements is dependent on the instrument, and without a GPS measurement to correct the predicted position, the navigation error grows over time [81]. For a UUV with a DVL-INS, a common navigation error is 0.5 - 2 % of the distance travelled [65]. More expensive INS systems can reduce navigation error to 0.1 % [65].

For a comprehensive summary and comparison of methods, Leonard et al. discuss the main options for underwater navigation for UUVs: GPS, acoustic transponders, map-based navigation, proprioceptive sensing, and cooperative navigation with many vehicles. In addition, Kinsey et al. provide a survey of navigation technology in UUVs – particularly enabling sensor technology and algorithms [64]. Kinsey et al. also touch on the challenges of navigation technology such as environmental estimation and multi-vehicle coordination [64].

Although the acoustic transponder and DVL-INS systems benefit the vehicle's navigation accuracy, they also make it susceptible to acoustic detection since they rely on active sonar.

2.2 Applications of UUVs

Unmanned underwater vehicles are autonomous platforms that can perform tasks that are considered "dull, dirty, and dangerous" for traditional maritime assets like ships and divers. Similar to unmanned systems in air and land domains, UUVs are changing the battlespace with their capabilities. About a half dozen European countries and China, DPRK, and Russia now have UUVs [74]. In the United States, the potential of UUVs and what they can do for the modern Navy has spurred many studies and calls for proposals to develop technology in UUVs [97]. In fact, on February 3, 2016, former Secretary of Defense Ashton Carter told sailors on the *USS Princeton* aircraft carrier that the US was going to invest $ 600 million in unmanned undersea vehicles over the next five years [80].

2.2.1 Current Missions

At present, UUVs are common tools for the defense industry, performing missions such as intelligence, surveillance, and reconnaissance (ISR), mine countermeasures (MCM), anti-submarine warfare (ASW), inspection, oceanography, payload delivery, time critical strike, and communication nodes [97].

Historically, the main roles of UUVs in defense are mine reconnaissance and ISR, especially mapping [97] [10] [74]. The robotic platforms can be equipped with sensors to evaluate oceanographic features and water column data including bathymetry, chlorophyll fluorescence, and optical backscattering [100] [97].

More recently, UUVs have been widely deployed for ASW. As an example, the NATO Centre for Maritime Research and Experimentation (CMRE) demonstrated a network of buoy and mobile UUVs with towed arrays which worked collaboratively to track submarines [84]. Similarly, ONR invested in Persistent Littoral Undersea Surveillance Network (PlusNet), an acoustic network of UUVs with towed arrays that used advanced autonomy like environment adaptability [54]. US Navy Admiral Jay Donnelly commented in October 2010 that with PlusNet, "Eventually, unmanned undersea vehicles and distributed netted sensors will likely replace our permanent fixed undersea sensor infrastructure, which in many cases is beyond its design life" [23].

2.2.2 Future Missions

Similar to unmanned systems in other domains, UUVs are changing the battespace with autonomy risk reduction, low profile, and low-effort deployability [97]. In the future, as energy options and autonomy improves, UUVs will be more capable of complex missions. UUVs could perform deception (jamming), act as training targets, counter other UUVs, perform surface action group interdiction, and control choke points [97] [35] [42]. The UUVs could expand their sizes to different applications from 3 in to 7 ft wide [35]. The UUV requirements to accomplish future missions is outlined in the U.S. Chief of Naval Operations' report to Congress, "Autonomous Undersea Vehicle Requirement for 2025" [70]. The U.S. Navy predicts that ultimately, UUVs could detect, track, and destroy an enemy, all autonomously [97].

Another example of modern UUV technology is using bistatic acoustic sensing: a fleet of

UUVs with acoustic receivers could evaluate a target with active sonar emitted by a single UUV [68] [57].

Furthermore, investing in the infrastructure to support UUV missions will also make UUVs more capable. The U.S. has already begun investing in equipping large UUVs to deploy small UUVs, submarines to launch UUVs, and charging stations in the ocean that UUVs could use to refuel [25] [48] [82].

2.3 Motivation for Detecting and Tracking UUVs

Prior to advances in low-SWAP sensors and autonomy, UUVs played a role strictly in mine reconnaissance and oceanography [97] [10] [74]. Today, they have evolved into a tool for smart mining and anti-submarine warfare [37] [74] [57]. Because UUVs are low-cost and easily deployable, they can be leveraged by less-established navies [74]. In fact, unmanned systems in general play a role in asymmetric warfare, a war between two parties with capabilities that are unbalanced [72]. UUVs, like air and ground unmanned systems, can perform persistent missions, in difficult locations like littoral waters, all with out risk to personnel. UUVs pose a threat of being as effective at sea denial as mines, a common tool in asymmetric warfare [22]. In comparison to mines, UUVs can operate anywhere and travel to a specific location. Existing defense systems that rely on change detection to find mines would not work against UUVs.

The existing ASW system also falls short when applied to protecting against UUVs. The ASW system relies on an indicator and warning system which alerts when submarines are leaving certain ports [62]. This informs ASW operators on what areas to search. UUVs, however, can be discreetly deployed anywhere, such as from a small military or civilian boat. This uncertainty of the starting location increases the area of possibility of where the UUV could be or travel to [74].

In addition, UUVs work autonomously and usually are single-mission. As a consequence, they do not require constant communication like a submarine or ship from a ground station [74]. Therefore, UUVs do not have as large a vulnerability with communication as would a submarine [74].

There is a growing concern that armed UUVs pose a problem to existing defense systems because they are hard to detect [30] [4] [74]. The missions of UUVs that are a concern are:

tracking and trailing ships and submarines; sensor deployment and ISR collection in home waters; and monitoring chokepoints and ports. In order to safeguard harbors, ships, and submarines, from the new threat of autonomous underwater vehicles, counter-UUV technology is critical.

As proof of this growing trend, the U.S. Navy has published strategic plans of investing in UUVs and several U.S. defense organizations have put out a call for proposals for new technology to counter UUVs.

2.3.1 U.S. Navy

The "UUV Master Plan" and "Autonomous Underwater Vehicle Requirement for 2025" are just two examples of influential reports made by the U.S. Navy to advocate for investing in UUV technology. The purpose of the "UUV Master Plan" was to define UUV capabilities such as the kinds of missions they can accomplish, define vehicle classes for each capability, and describe technology advances and readiness levels in order to fulfill these capabilities [97]. The US Navy Undersea Warfare Division (N97) published a report to congress called "Autonomous Underwater Vehicle Requirement for 2025" which described a network of fixed and mobile underwater sensors, undersea charging stations, and other support systems for UUVs [35].

Also a part of the U.S. Navy, the Strategic Systems Program for Nuclear Weapons Security has put out a SBIR for "Unmanned Undersea Vehicle (UUV) Detection and Classification in Harbor Environments" [4]. They are interested in investing in technology that can detect UUVs in ports and harbors [4]. The existing techniques like change detection apply to stagnant threats like mines. UUVs, on the other hand, are mobile and can be armed [4]. The requirements of the SBIR are: a standoff distance of 1000 m with a false alarm tolerance of one per day, a proposed system that is easily integrated into current harbor protection systems, and a fast reaction time to detect UUVs [4].

2.3.2 DARPA

In 2016, DARPA Tactical Technology Office program sent out a Broad Agency Announcement for an "Open Ocean Counter UUV Study" [30]. They invited researchers to identify all

potential vulnerabilities of UUVs as well as come up with ways to detect and negate UUVs [30]. The detection system would ideally find UUVs at far ranges, track multiple vehicles, and characterize the UUVs [30]. The second part of the program would invest in novel technology to stop or capture another vehicle [30]. DARPA mentions that UUV vulnerabilities include but are not limited to their energy limits, navigation errors, command and control limitations, limited autonomy, and propulsion system [30].

In addition, DARPA has initiated a program in 2017 for UUVs for ASW applications [36]. The DARPA program Mobile Off-board Command, Control and Attack (MOCCA) includes UUVs working together with submarines to find enemy submarines [36] [91]. The UUV will travel away from the main submarine to use active sonar and detect enemy submarines [36]. This concept of operations is ideal because the main submarine will not be detected and enemy submarines can be detected at greater ranges [45]. For this program, DARPA has awarded BAE 4.6 million dollars [36].

2.3.3 Rapid Reaction Technology Office

The Defense for Research and Engineering Rapid Reaction Technology Office has also put out a request for counter-UUV technology as part of the Stiletto Maritime Demonstration Program [2]. They are investing in acoustic technology that can detect classify and track UUVs in shallow waters [2]. Their concern is that UUVs of malicious intent are operating in ports and harbors near U.S. Navy assets like ships [2]. Similar to the concern of the Strategic Systems Program for Nuclear Weapons Security, this organization mentions that existing systems intended to catch divers and swimmers have a delayed reaction to finding UUVs [2].

2.3.4 Defense Science Board

The Defense Science Board Task force created a report in 2016 on "Next-Generation Unmanned Undersea Systems" to find new capabilities of UUVs [42]. The group included a variety of experts from the U.S. Navy and research labs such as John Hopkins Applied Physics Laboratory [42]. The recommended missions from the study are choke point control, operation deception, ASW, and surface action group interdiction [42]. Along the same lines

as the creation of the Deputy Assistant Secretary of the Navy (DASN) Unmanned Systems (UxS) and Unmanned Warfare Systems (OPNAV N99), the task force recommended the creation of an undersea program led by the Office of the Under Secretary of Defense for Acquisition, Technology, and Logistics (OUSD (AT&L)) and the Assistant Secretary of the Navy for Research, Development and Acquisition (ASN (RDA)) that would accommodate more rapid development and deployment of UUVs [42].

All of these studies and proposals recognize the importance of investing in counter-UUV technology. In response to this gap in defense technology, this thesis presents one of the first demonstrations of detecting and tracking a UUV in a realistic ocean environment with passive acoustics.

Chapter 3

Related Work

Investing in counter-UUV technology is motivated by the concern that current defense systems in ships, harbors, and submarines cannot detect, track, or prevent armed UUVs from causing harm. In terms of boats and submarines, passive sonar detection and tracking has been well researched. Since the role of UUVs is changing to include smart mining and ASW, research in UUV detection and tracking has yet to be explored fully. To date, research has been done in minimizing the acoustic noise of UUVs to prevent interference with onboard passive acoustic sensors. Also, due to the increasing concern of UUVs collecting ISR data in harbors, research in complementing existing harbor surveillance systems has been done. Furthermore, tracking submarines and ships from UUVs equipped with passive sonar arrays has been demonstrated.

3.1 Acoustic Spectrum Analysis of UUVs

Ship, diver, and submarine acoustic signatures have been analyzed for harbor surveillance applications. UUV acoustic signatures have also been studied, but for a different purpose: understanding how UUV self-generated noise interferes with on-board passive acoustic sensors.

Holmes et al. give an overview of UUV acoustic signatures in the low- to mid-range frequencies [60]. The study was created to understand how UUV self-generated noise interferes with on-board acoustic sensors [60]. The authors describe previous work on measuring acoustic signatures of off-the-shelf vehicles: Remus-100, Autosub, Ocean Explorer,

and Odyssey-Oases [60]. The measurement techniques include securing a vehicle in a test tank with a bollard fixture [102] [59], on-board towed sensors [102] [59], and driving by a fixed vertical array [102] [53]. The authors concluded that sources of vehicle noise are electro-magnetic, mechanical (bearing, actuator), and caused by cavitation flow noise [60].

Florida Atlantic University researchers investigated techniques to minimize radiated noise specifically of an Ocean Explorer Class UUV [29]. In order to reduce acoustic noise, Florida Atlantic University measured and modeled vibration transmission paths of the Ocean Explorer Class UUV to understand its acoustic signature [28]. Naval Undersea Warfare Center (NUWC) has also done research on radiated self-generated noise of the Ocean Explorer UUV [29].

Inspired by improving harbor security, several studies have researched diver signatures. As summarized in Zhang et al., researchers at Naval Research Laboratory (NRL) investigated detecting open circuit breathing systems of divers in the San Diego harbor [101].

Small boats are also an area of interest for acoustic spectrum analysis. Northwest Electromagnetic and Acoustics Research Laboratory at Portland State studied acoustic signatures of small boats with passive sonar [76]. They analyzed the broadband noise by finding harmonic tones that related to the engine and propeller [76]. This method in signal processing is called harmonic extraction and analysis tool (HEAT) [76].

3.2 Automatic Target Recognition

The purpose of automatic target recognition (ATR) is to identify objects of interest in a cluttered environment with a sensor that has internal noise [33]. Decreasing a pilot's workload was the initial motivating factor for ATR. Instead of a human, a computer can do the detection and recognition. This is, however, a difficult technical problem because target signature and clutter can vary by situation [33].

ATR is used with imaging sensors like forward looking infrared radiometer (FLIR) and synthetic aperture radar (SAR) but can be applied to non-imaging sensors as well [33] . For instance, active and passive sonar techniques are widely used by the military to characterize ships and submarines [32].

3.2.1 Detection with Active Sonar

Zhang et al. discuss commercial active sonar ATR systems such as Northrop Grumman's Centurion harbor system and DRS Technology Sea Sentry [101]. Another ATR commercial system example is manufactured by RESON: an Integrated Underwater Intruder Detection system that uses active sonar to track divers [90].

Many of the off-the-shelf systems rely on active, high frequency sonar and target divers [101]. Despite the commercial availability of these systems, active sonar has many disadvantages: high cost, high false alarm rate, interference from multipath in shallow water, danger to marine life, and overtness [17]. For these reasons, Stevens Institute of Technology, Netherlands Organization for Applied Scientific Research (TNO), and others have researched passive acoustic alternatives.

3.2.2 Detection with Passive Sonar

Due to the role of submarines and ships in World War II, the research of detecting traditional maritime assets is well-established [24]. Today's research focus is on ship acoustic noise due to environmental concerns and passive acoustic harbor surveillance to protect against divers and small boats [24].

For finding and identifying ships, De Moura et al. use the technique, detection of envelope modulation on noise (DEMON), to find signal relevant features in passive sonar [32]. DEMON characterizes narrowband frequencies related to the number of shafts and rotation frequency of the ship's propulsion system [32]. Chung et al. show how this method can be applied to identifying ship signatures in a complicated environment like an urban harbor [24].

To improve harbor security, Stevens Institute of Technology partnered with the Netherlands Organization for Applied Scientific Research (TNO) to identify small boats and divers with passive acoustics [44]. They compared two passive systems – Stevens Passive Acoustic System (SPADES) and Delphinus [44].

Delphinus is typically used for marine mammals and is towed behind a surface ship [44]. The SPADES set-up includes four hydrophones spaced between 0 m and 100 m, and a central unit secured on the sea floor [44]. They tested a range of acoustic target signatures of boats and divers [44].

Furthermore, TNO has specifically looked into passively tracking a closed-circuit underwater breathing apparatus in a harbor environment [43]. Their motivation to use passive sonar is from the reverberation caused by active sonar in a harbor environment and restrictions on acoustic regulations for protecting marine life [43].

In addition, the Stevens Institute of Technology characterized the source level of divers to find possible detection distances in different background noise levels, including ship traffic [17].

3.3 Passive Acoustic Tracking

Since the cold war, passive sonar tracking has been the main technique for submarines to track surrounding targets but remain stealth. Passive sonar is also advantageous for not disrupting marine life, avoiding multipath propagation and interference, and driving down costs [49].

Brinkmann et al. illustrate how passive sonar is used on submarines to detect and range other platforms: submarines are equipped with a cylindrical hydrophone array on the bow, flank arrays on the sides, and a towed array off the back [20]. For passive sonar, bearing tracks are inputted into a target motion analysis (TMA) [20]. This analysis estimates bearing, speed, and range of the target [20]. Therefore, the operator can get a global perspective of platforms nearby [20]. In the case of Brinkman et al., they are developing automatic tracking of broadband targets for the purpose of relieving the operator of initialization, maintenance, and deletion of target tracks.

Passive sonar tracking has also been integrated onto UUVs for the purpose of ASW. Kemna et al. implemented a cooperative active ASW network using UUVs [63]. They programmed UUVs to "hold at risk" – where they monitor all submarines leaving a port or chokepoint [63]. Similar work had been done in collaborative autonomous underwater vehicles with passive sonar at MIT [41] [39] [40] and at Virginia Tech [71].

The "Passive Acoustic Threat Detection System" developed by Stevens Institute of Technology is another example of leveraging UUVs to track threats. At Stevens, they investigated localizing the threat to cue a UUV to investigate the source [34]. To accomplish this, they used a hydrophone system to measure the correlation between the signals that mimicked a UUV, diver, and boat [34]. Then, after localizing the threat, the researchers cued a UUV

to investigate the noise source [34].

In terms of tracking UUVs, Gebbie et al. demonstrated passively tracking a UUV with a bottom mounted horizontal line array hydrophone system [50]. They tracked an underway REMUS-100 by its acoustic doppler current profiler (ADCP), broadband modem noise, and a single strong frequency from the propulsion system [50]. The same research group characterized the acoustic profile of the REMUS-100 with an onboard acoustic modem, which they used in OASES, propagation modeling software, to predict transmission loss and multipath arrival of the signal [86].

Related to tracking UUVs, work has been done in detecting noisy surface targets like small boats and analyzing the multipath arrivals on a passive acoustic array [51] [52].

Although the research area of passive acoustic detection and tracking is well-established for traditional maritime platforms – ships, submarines, and even divers – UUVs are grossly unexplored. The concern of armed UUVs did not exist ten years ago, so there was no prior need to investigate counter-UUV technology.

This thesis addresses this gap in counter-UUV technology by presenting the first demonstration of detecting and tracking a UUV strictly by its self-generated noise. On the topic of detection, this thesis is the first to accomplish detecting a UUV in field experiments with cluttered environments. This thesis quantifies the advantage of applying spectral filters, derived by the vehicle PSD estimate, to detect the vehicle's presence. The only other demonstration of UUV tracking was presented in Gebbie et al [50]. In this work, a REMUS-100 was tracked with a single tone of 1065 Hz. This experiment, however, had less clutter, broadband background noise, and boat interferers than the Charles River experiment in this thesis. As shown in the detection results of this thesis, using multiple, high frequencies is more effective in identifying UUVs in realistic environments. The tracking results in this paper were the result of beamforming on multiple frequencies.

This thesis also presents the first micro-UUV power spectral density estimate with time analysis, showing how frequencies of the electro-mechanical noise fluctuate.

Chapter 4

Detection and Tracking Theory

Detecting and tracking the presence of a UUV through passive sonar in a realistic environment was accomplished through energy detection thresholding, spectral filtering, and beamforming.

4.1 Detection Threshold Theory

In passive sonar, an observer listens to signals being emitted by a target [31]. The signal is picked up by a hydrophone which converts changes in sound pressure levels to electrical signals [31]. In order to determine if the target is present, the signal to noise ratio (SNR) is calculated [31]. If the SNR is greater than a set detection threshold, then the operator perceives the target as being present [31].

4.1.1 Passive Sonar Equation

The signal to noise ratio of the target at the receiver hydrophones can be approximated by the sonar equation, all of which are parameters in decibels [31]:

$$SE = SL - PL - NL + AG - DT \text{ [31]}.$$

SE is the signal excess that corresponds to the probability of detection [31]. SL is the source level which is referenced at 1 m from acoustic source [31]. PL is propagation loss due to the distance that the signal has to travel to the receiver [31]. NL stands for noise level of the background. AG represents array gain and finally, DT is the detection threshold [31].

The mathematical definition of detection threshold is

$$DT = 10log_{10}(S/N) \text{ [31]};$$

S is the signal power in the receiver bandwidth (mean squared voltage), similarly N is the noise power in the receiver bandwidth (mean squared voltage) [31].

4.1.2 Receiver Operating Characteristic Curves

To calculate the ideal detection threshold, receiver operating characteristic curve (ROC) analysis is performed.

To begin, there are binary options, summarized in Table 4.1, for detecting the presence of a UUV in a noisy environment: signal present, signal not present [96]. The decision of the detection algorithm will be a correct detection, missed detection, false alarm, or correct no detection [96]. These options are representative of the probabilities of detection, $p(D)$, and false alarms, $p(FA)$, as presented in Table 4.1.

		Decision / Hypothesis	
		Signal Present	**Signal Not Present**
Actual Input	**Signal Present**	Correct Detection p(D)	Missed Detection p(Miss)=1-p(D)
	Signal Not Present	False Alarm p(FA)	Correct No Detection p(Null)=1-p(FA)

Table 4.1: Detection algorithm decisions and probability definitions: the result of the detection algorithm will either be a correct detection, false alarm, missed detection, or correct no detection.

By changing the detection threshold, one can calculate the probability of detection and probability of false alarm [96]. By plotting all thresholds, one can find the ideal detection threshold that will maximize detection but minimize false alarms [96].

This plot is called a receiver operating characteristic (ROC) curve, where the ideal detector has zero false alarms (low probability of false alarms) and always detects (high probability of detection) [98]. The ROC curve was first used during World War II for detecting planes with radar [98]. The plot is normalized so the probabilities range from 0 to 1 [98]. Another property of the ROC curves is their dependence on the signal and noise strength [98].

A measure of accuracy of a ROC curve is the area under the curve [8]. Recall, that the desired outcome is perfect detection and zero false alarms. Therefore, the ideal area under

the curve of a normalized ROC curve is 1. The closer to 1, the more accurate the ROC curve [8]. The trapezoidal method for estimating the area under the ROC curve was used in this thesis [11].

In order to find the optimal detection threshold, the distance to the optimal case, a probability of detection equal to one and a probability of false alarm equal to zero, was found:

$$d = \sqrt{(1 - sensitivity)^2 + (1 - specificity)^2}[8].$$

The true positive rate, or probability of detection, is also considered the *sensitivity* of the detector [8]. *Specificity* of the detector is the probability of no false alarms; or

$$Specificity \ = \ 1 - P(FA) \ [8].$$

This is related to the Youden index which is

$$Youden\ Index = sensitivity \ + \ specificity - 1$$

where the higher the Youden index, the better the detection [8].

4.2 Power Spectral Density

To extract the signal of the UUV from background noise, it is important to first understand the signal distribution in the frequency domain [77]. Expected instantaneous power is defined as [77]:

$$E[x^2(t)] = R_{xx}(0) = \frac{1}{2\pi} \int_{-\infty}^{\infty} S_{xx}(j\omega)d\omega,$$

where *x(t)* is the incoming signal on the hydrophone, S_{xx} is the power spectral density (PSD) of *x(t)* and the continuous Fourier transform of the autocorrelation function is R_{xx} [77]. The PSD can be estimated with the Einstein-Wiener-Khinchin theorem:

$$R_{xx}(\tau) \Leftrightarrow S_{xx}(j\omega) = \lim_{T\to\infty} \frac{1}{2T} E[|X_T(j\omega)|^2] \ [77].$$

This theorem comes from taking a windowed function, $w_T(t)$, applied to the signal, *x(t)*, so that it is only defined on the period, T:

$$x_T(t) = w_T(t)x(t) \ [77].$$

The energy spectral density (ESD) is defined as

$$\bar{S}_{xx}(j\omega) = |X_T(j\omega)|^2 \text{ [77]}.$$

After dividing by the period, *2T*, the expression becomes a periodogram:

$$\frac{1}{2T}|X_T(j\omega)|^2 \text{ [77]}.$$

Taking the limit as the period, T, goes to infinity, this result approaches the power spectral density, resulting in the Einstein-Wiener-Khinchin theorem [77].

This means that for large periods of T, the frequency resolution will improve [77]. By averaging over many realizations of the random process *x(t)* for a given period, T, the estimate of the power spectral density will improve [77].

In this thesis, the power spectral density of a UUV was found by collecting acoustic data of the vehicle in a quiet pool environment.

4.3 Underway Vehicle Detection

In order to determine the presence of a vehicle in a realistic environment, short-time Fourier transform was performed, a spectral filter applied, and the energy calculated.

4.3.1 Short-Time Fourier Transform

Since the process of detecting the vehicle is a function of time, discrete Fourier transform (DFT) was performed on over-lapping short time periods. This is demonstrated in Figure 4-1. The incoming signal, $x(t)$, is multiplied by a window function, $w(t)$, so that the signal is divided into time segments. Following the segmentation of the signal, DFT was applied to each snapshot.

4.3.2 Energy Calculation

Acoustic energy from the UUV self-generated noise was calculated by taking the integral of the energy spectral density over all the frequencies [26]:

$$E = \frac{1}{2\pi}\int_{-\infty}^{\infty}|F(j\omega)|^2 d\omega,$$

where $|F(j\omega)|^2$ is the energy spectral density of $f(t)$ [26].

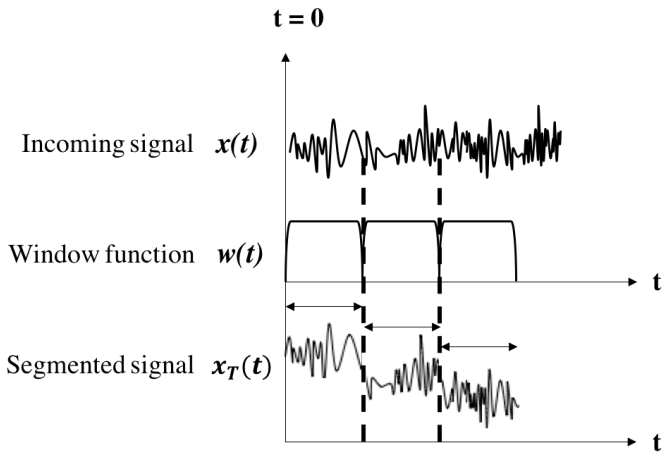

Figure 4-1: Windowing effect on incoming signal $x(t)$: when a window function, $w(t)$, is applied to the signal, the signal becomes segmented, which is used for short-time Fourier transform [55].

4.3.3 Spectral Filters

The advantage of applying a spectral filter to an incoming signal is that one can change the relative amplitude of frequencies that are important – and even eliminate an unwanted frequency band entirely [78].

Since the vehicle revealed strong narrowband frequencies, two filters were applied to improve the signal to noise ratio of the UUV: a bandpass filter and the vehicle PSD estimate as a filter. A bandpass filter is an example of a frequency-selective filter. It will pass a small range of frequencies, but attenuate the others not specified in that range, as seen in Figure 4-2 [78].

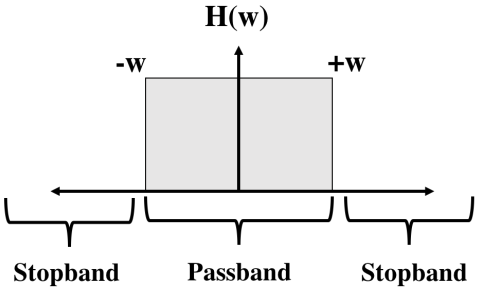

Figure 4-2: Frequency response of ideal low pass filter: frequencies that are passed through are between positive and negative w, frequencies that are eliminated are represented by the stop-band [78].

The prominent high frequencies found in the PSD estimate of the vehicle were used as the defining frequencies of the bandpass filter.

The other filter applied to the data is a frequency-shaping filter [78]. Using the PSD estimate over the entire frequency domain as a filter shaped the frequencies of the input signal, increasing the amplitude of important frequencies of the UUV and diminishing undesired frequencies of the UUV.

Frequency filters can be conveniently applied to the incoming signal with the multiplication-convolution property of Fourier transforms [78]. Starting with the signal, $x(t)$, and the filter, $h(t)$, the outgoing filtered signal, $y(t)$, is

$$y(t) = x(t) * h(t) \text{ [78].}$$

Transforming this into the frequency domain, the expression becomes

$$Y(\omega) = X(\omega)H(\omega) \text{ [78].}$$

These filtering concepts were effective in increasing the SNR of the vehicle acoustic signal in the background noise of the Charles River and Jenkins Pond.

4.3.4 Summary

In practice, a short-time Fourier transform was performed on the incoming signal, a filter was applied to increase the SNR of the vehicle acoustic signature, and energy was calculated to determine the presence of the vehicle. This is summarized in Figure 4-3.

The ROC curves were produced based off of various detection thresholds. The probability of detection, $P(D)$, and false alarms, $P(FA)$, were calculated from an experiment where the presence of the vehicle was known. Thus the $P(FA)$ and $P(D)$ were calculated over the whole experiment run. Ultimately, the ideal detection threshold was found from the ROC curves.

For future exercises, the calculated ideal detection threshold would be used, but considerations of the target source level, background noise, and distance of target should all be taken into account as specified in the passive sonar equation.

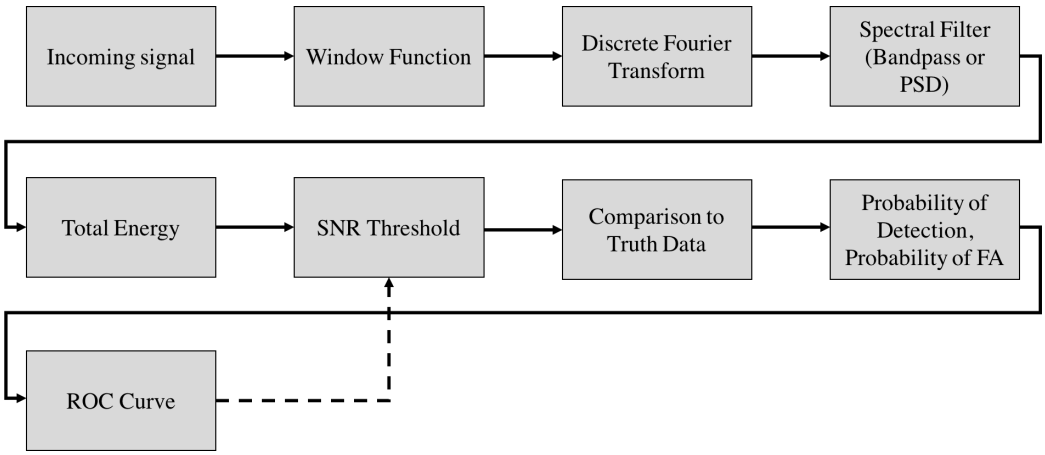

Figure 4-3: Process for producing ROC curves on a moving target: incoming data from a hydrophone element is analyzed by applying short-time Fourier transform, spectral filtering, and energy thresholding. The result is compared to the true presence of the UUV to calculate probabilities of false alarms and true detections.

4.4 Beamforming

The second part of the analysis involves tracking the direction of arrival of the UUV self-generated noise. This is accomplished through beamforming, over time, on a horizontal line array. This section begins by describing beamforming of a single time snapshot of data. The following section describes the process for performing beamforming over time.

4.4.1 Uniform Linear Arrays

The purpose of an array is to filter signals in the space-time field by finding their spatial characteristics [94]. These characteristics are a function of an angle or wavenumber, where wavenumber is defined as

$$\vec{k} = -\frac{2\pi}{\lambda}\begin{bmatrix} \sin(\theta)\,\cos(\phi) \\ \sin(\theta)\,\sin(\phi) \\ \cos(\theta) \end{bmatrix}$$

in the domain pictured in Figure 4-4.

Line arrays, as used in this thesis, resolve angle in only one direction [94]. When there is equal distance spacing of elements on a line array, this is called a "uniform linear array," pictured in Figure 4-5 [94].

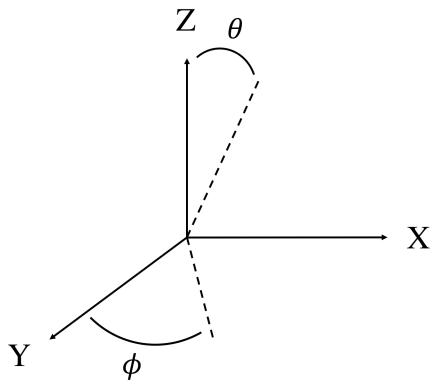

Figure 4-4: Coordinate system for beamforming: elevation and azimuth are defined as θ and ϕ respectively.

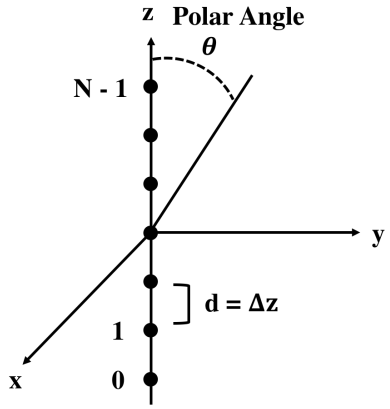

Figure 4-5: Coordinates and element spacing of a line array: a vertical line array measures direction of arrival in elevation, or θ. The elements, which are identified by numbers 0 to N are evenly spaced by Δz [94].

The locations of the elements are defined as

$$p_{z_n} = (n - \tfrac{N-1}{2})d,\ n = 0, 1, ..., N-1 \text{ [94]}.$$

The signal on each element is defined as a vector where each row is a location p_n,

$$\vec{f}(t, p_n) = \begin{bmatrix} f(t, p_0) \\ f(t, p_1) \\ \vdots \\ f(t, p_{N-1}) \end{bmatrix}$$

The array output $y(t)$ is defined as applying a filter, the impulse response, $h(t)$, in this case, to each array element signal, $f_n(t, p_n)$, and summing them together:

$$y(t) = \Sigma_{n=0}^{N-1} \int_{-\infty}^{\infty} h_n(t-\tau) f_n(\tau, p_n) d\tau$$

This order of operations is presented in visual form in Figure 4-6.

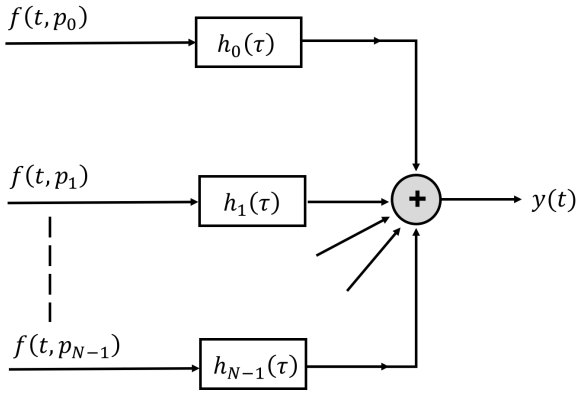

Figure 4-6: Filtering process of an array in visual form: the incoming signal on each element of the array $f(t, p_n)$ is filtered by $h_n(\tau)$ and summed together to produce the array output $y(t)$ [94].

The array output can also be written compactly in the frequency domain with vectors:

$$Y(\omega) = \vec{H}^T(\omega)\vec{F}(\omega)$$

where

$$\vec{H}(\omega) = \int_{-\infty}^{\infty} \vec{h}(t) e^{-j\omega t} dt,$$

and

$$\vec{F}(\omega, \vec{p}) = \int_{-\infty}^{\infty} f(t, \vec{p}) e^{-j\omega t} dt [94].$$

For a plane wave input, the delay, τ, between the elements of the array is a function of their spatial dependence,

$$\vec{f}(t, \vec{p}) = \begin{bmatrix} f(t-\tau_0) \\ f(t-\tau_1) \\ \vdots \\ f(t-\tau_{N-1}) \end{bmatrix}$$

where

$$\tau_n = \frac{\vec{a}^T p_n}{c} \text{ [94].}$$

In three dimensions, the direction vector, $\vec{a}$, is

$$\vec{a} = \begin{bmatrix} \text{-sin}(\theta)\ \cos(\phi) \\ \text{-sin}(\theta)\ \sin(\phi) \\ \text{-cos}(\theta) \end{bmatrix}$$

but in the case of a vertical line array, as pictured in Figure 4-5,

$$a = cos(\theta).$$

The nth component of $F(\omega)$ is

$$F_n(\omega) = e^{-j\omega\tau_n} F(\omega),$$

which is a function of the original signal multiplied by a complex exponential of the delay [94].

Next, the delay is rewritten in terms of the wavenumber

$$\omega\tau_n = \vec{k}^T p_n,$$

where the wavenumber is

$$k = -\tfrac{2\pi}{\lambda} cos(\theta)\ [94].$$

The incoming signal on the array can then be written in terms of an array manifold vector,

$$\vec{v}_k(\vec{k}) = \begin{bmatrix} e^{-j\vec{k}^T p_0} \\ e^{-j\vec{k}^T p_1} \\ \vdots \\ e^{-j\vec{k}^T p_{N-1}} \end{bmatrix}$$

so it simplifies to

$$\vec{F}_\omega = F(\omega)\vec{v}_k(\vec{k}).$$

Finally, a common delay is applied to each element. This process, called "conventional beamforming" or "delay-and-sum beamforming," is depicted in Figure 4-7 [94].

The filter is

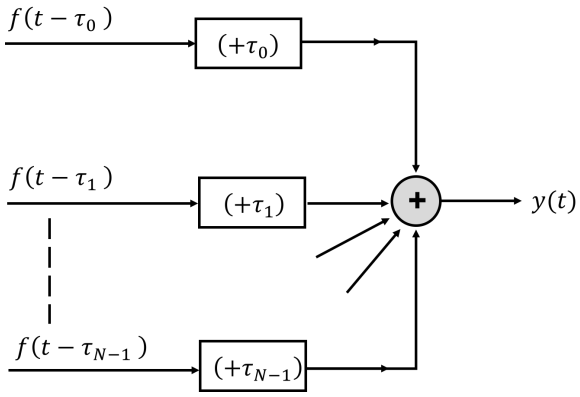

Figure 4-7: Delay and sum beamforming process in visual form: the signal on each element of the array, $f(t-\tau_n)$, is filtered by applying a delay, $h_n(\tau)$, and summed together to produce the array output $y(t)$ [94].

$$h_n(\tau) = \frac{1}{N}\delta(\tau+\tau_n) \text{ [94].}$$

The beamforming process can be written more compactly as

$$\vec{H}^T(\omega) = \frac{1}{N}\vec{v_k}^H(k_s)$$

where k_s is the desired steering angle [94]. Putting it altogether, the array response is, in the frequency domain,

$$Y(\omega,\vec{k}) = \vec{H}^T(\omega)\vec{v_k}(\vec{k}),$$

also known as the frequency-wavenumber response function.

In the situation where the signal is narrowband, the delay is actually a phase shift. Therefore, the gain and phase shift as shown in Figure 4-8, can be adjusted to achieve an optimal beamformer.

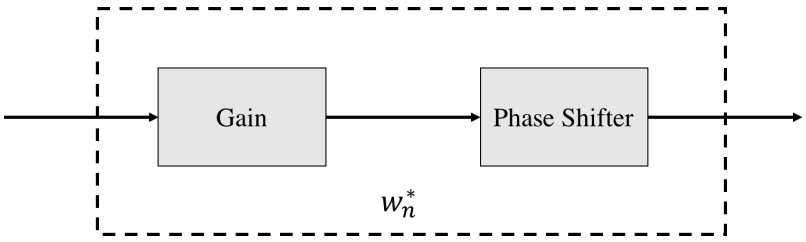

Figure 4-8: Weights for a narrowband beamformer: gain and phase can be modified to create an optimal beamformer [94].

The complex weight vector that acts as the gain and phase shifter is

$$\vec{w}^H = [w_0^* \quad w_1^* \quad ... \quad w_{N-1}^*],$$

so that the frequency wavenumber response is

$$Y(\omega, \vec{k}) = \vec{w}^H \vec{v_k}(k)$$

and

$$\vec{w}^H = \vec{H}^T(\omega_C) \text{ [94]}.$$

To transform the frequency-wavenumber function into a beampattern, the wavenumber is put into terms of an angle that only exists on the visible spectrum. For a uniform linear array this is

$$B_\theta(\theta) = \vec{w}^H \vec{v_\theta}(\theta) = e^{-j(\frac{N-1}{2})\frac{2\pi d}{\lambda}cos(\theta)} \Sigma_{n=0}^{N-1} w_n^* e^{jn\frac{2\pi d}{\lambda}cos(\theta)}$$

with

$$0 \leq \theta \leq \pi \text{ [94]}.$$

4.4.2 Weighted Linear Arrays

Optimizing the weights of a beampattern can improve the beampattern by narrowing the beamwidth or decreasing the side lobes.

Uniform Weighting

In the uniform weighting case, seen in Figure 4-9, the weights are

$$w_n = \frac{1}{N}, n = 0, 1, ...N-1$$

and the beampattern is

$$B_\theta = \frac{1}{N} \frac{sin(\frac{N}{2}\frac{2\pi}{\lambda}cos(\theta)d)}{sin(\frac{1}{2}\frac{2\pi}{\lambda}cos(\theta d))},$$

with

$$0 \leq \theta \leq \pi \text{ [94]}.$$

For uniformly weighted linear arrays, the null-to-null beamwidth, BW_{NN}, is

$$BW_{NN} = 2\frac{\lambda}{Nd} \text{ [94]}.$$

For the case of

$$d = \lambda/2,$$

the beamwidth becomes

$$BW_{NN} = 2sin^{-1}(2/N),$$

which is in the theta-space [94].

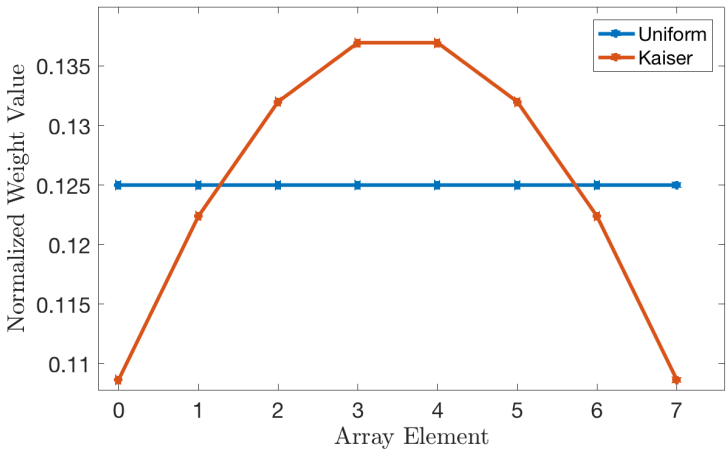

Figure 4-9: Comparison of Kaiser and uniform weights: the tradeoff between Kaiser and uniform weights is side lobe height and beamwidth. Kaiser weighting decreases side lobe heights but widens the beamwidth [94].

Kaiser Weighting

To decrease the side lobes of the beampattern, Kaiser weighting, pictured in Figure 4-9, was applied to the array datasets of the Charles River and Jenkins Pond experiments.

This effect, a decrease in side lobes, is apparent in Figures 4-10 and 4-11, which are the theoretical beampatterns of the Charles River and Jenkins Pond experiments. The theoretical beampatterns were derived with the experiment configurations summarized in Table 4.2.

4.4.3 Array Steering

The goal of using beamforming is to find the direction of the noise source, which is not always at broadside, and could be, in fact, moving over time. Therefore, the beampattern is steered across many look angles to find the maximum response.

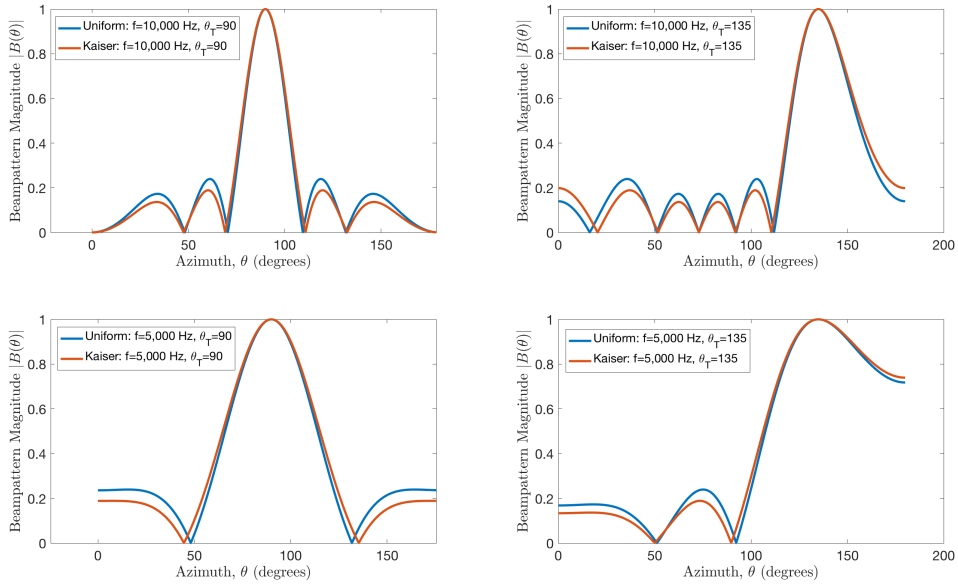

Figure 4-10: Theoretical beampatterns of Charles River array configuration: in each subplot, uniform (blue) and Kaiser (red) weightings are compared. The top figures are beampatterns at 10,000 Hz, the cutoff frequency for spatial aliasing in this configuration. The bottom figures are beampatterns at 5,000 Hz, half of the cutoff frequency for spatial aliasing. The left plots are steered to broadside or 90^o, the right plots are steered to 135^o.

Array Specifications	Symbol	Jenkins Pond	Charles River
Number of Elements	N	8	6
Element spacing [m]	d	0.25	0.075
Cutoff frequency for spatial aliasing [Hz]	f_c	3,000	10,000
Null-Null Beamwidth [degrees]	BW_{NN}	28	38

Table 4.2: Array specifications used in the Jenkins Pond and Charles River experiments: the Jenkins Pond array had a wider aperture than the Charles River array due to the increase in the number of elements and element spacing; however, it had lower cutoff frequency for spatial aliasing.

To begin, the steering direction is defined in the wavenumber space as

$$k = k_T,$$

with uniform weighting the beampattern becomes

$$B(k : k_T) = \tfrac{1}{N} v_k^H(k_T) v_k(k) \text{ [94].}$$

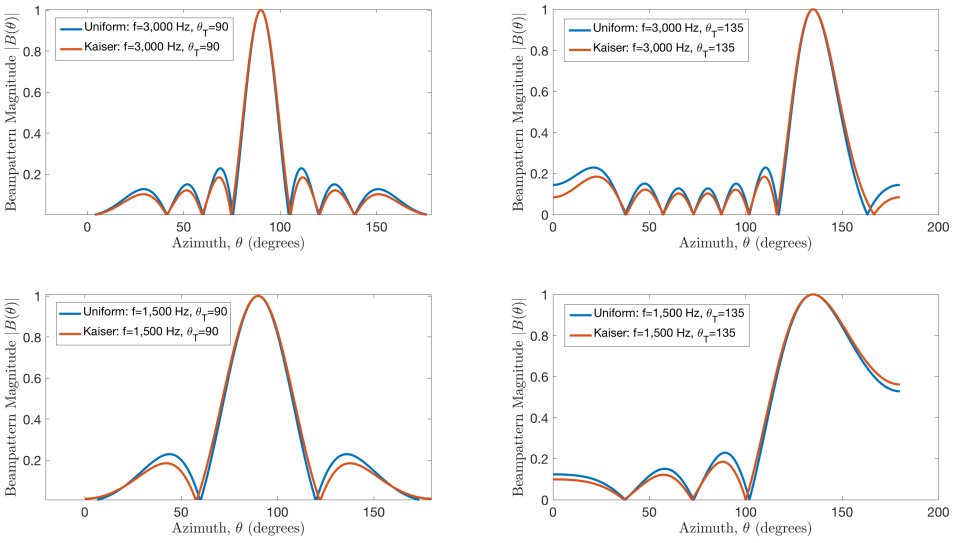

Figure 4-11: Theoretical beampatterns of Jenkins Pond array configuration: in each subplot, uniform (blue) and Kaiser (red) weightings are compared. The top figures are beampatterns at 3,000 Hz, the cutoff frequency for spatial aliasing in this configuration. The bottom figures are beampatterns at 1,500 Hz, half of the cutoff frequency for spatial aliasing. The left plots are steered to broadside or 90^o, the right plots are steered to 135^o.

In angle-space, this conventional beampattern is

$$B_{\theta C}(\theta : \theta_T) = \frac{1}{N} \frac{sin(\frac{\pi N d}{\lambda}(cos(\theta) - cos(\theta_T))}{sin(\frac{\pi d}{\lambda}(cos(\theta) - cos(\theta_T)))} \text{ [94].}$$

As an example of steering, the right-most subplots of the theoretical beampatterns in Figures 4-11 and 4-10 of the experiments are steered to 135^o. As the main lobe moves towards end-fire, the beamwidth increases.

4.4.4 Beamforming on a Moving Target

For estimating the bearing of a moving, broadband noise source, such as a UUV, beamforming is applied on overlapping time segments, on individual frequencies, and across many look angles. The ultimate result is a peak array response at certain angles as a function of the time segments.

Similar to the starting process of detecting the vehicle's presence over time using energy, short-time discrete Fourier transform (DFT) is applied to the array data, segmenting the entire dataset into overlapping snapshots of time.

To apply narrowband beamforming, the frequencies are individually analyzed. For each frequency of interest, beamforming is applied across all steering angles. Next, the individual frequency array response results are averaged. Then this process is repeated for every time segment. Figure 4-12 is an overview of this process.

Finally, the maximum array response over time was smoothed using a loess fit: local regression performed with a second degree polynomial model and weighted linear least squares [3].

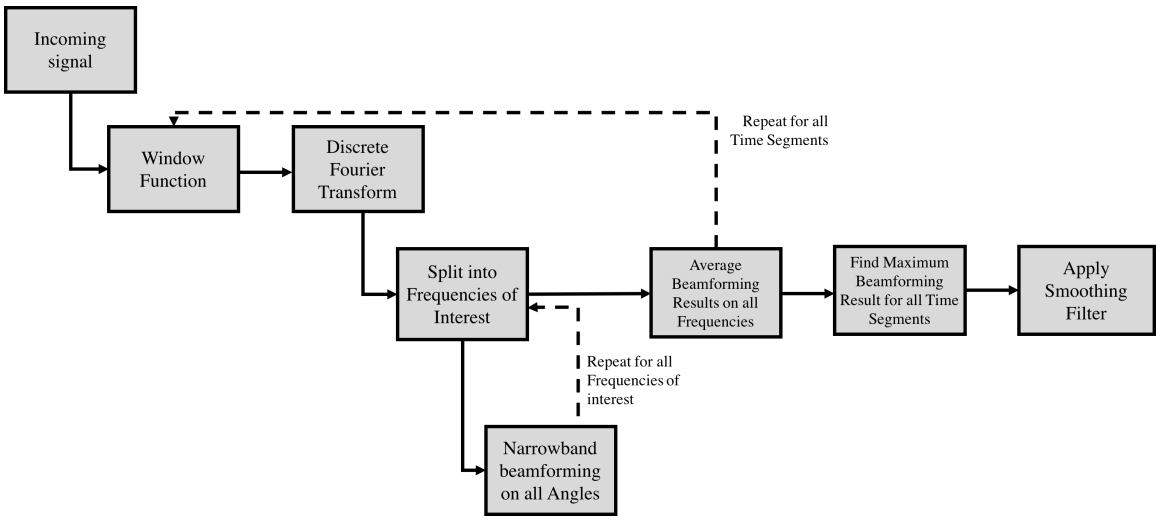

Figure 4-12: Beamforming process for a moving target: to estimate bearing of a moving target, the incoming signal on each array element is segmented into time snapshots, discrete Fourier transform is applied, and frequencies are individually beamformed. The beamformer results across all frequencies are averaged, resulting in a beamformer output over time.

4.4.5 Minimum Power Distortionless Response (MPDR) Beamformer

To improve the beamformer output, the minimum power distortionless filter was applied. This filter leverages having an estimate spectral matrix, $S_x(\omega)$, of the signal, $x(t)$, but not an estimate of the spectral matrix of the noise, $S_n(\omega)$ [93].

When steering in the direction of the signal, the MPDR filter is the same as the minimum variance distortionless response (MVDR) [93].

To find the spectral matrix of the signal, $X(\omega)$, the array data must be first processed

using the time-snapshot model used in detection and conventional beamforming. The signal is segmented by periods of ΔT so that its Fourier transform is defined as

$$X_{\Delta T}(\omega_m) = \frac{1}{\sqrt{\Delta T}} \int_0^{\Delta T} x(t) e^{-j(\omega_c + m\omega_\Delta)t} dt$$

where

$$\omega_m = \omega_c + m\omega_\Delta$$

is the centered frequency with $\Delta\omega$ frequency resolution, and

$$\omega_\Delta = \frac{2\pi}{\Delta T}$$

is a function of the snapshot length, ΔT [92].

The covariance matrix is

$$S_{X,\Delta T} = E[X_{\Delta T}(\omega_m) X_{\Delta T}^H(\omega_m)].$$

From the Wiener-Khinchin theorem, for long snapshot periods, ΔT, the true spectral matrix of the process can be estimated with the snapshot model:

$$\lim_{\Delta T \to \infty} [S_{x,\Delta T}(m,m)]_{nn} = S_x(\omega_c + m\omega_{\Delta T})]_{nn} \text{ [92]}.$$

For a plane-wave signal in noise, like the case of the UUV noise in the ocean, the incoming signal, $X(\omega)$, is broken up by noise and signal:

$$X(\omega) = F(\omega)\vec{v}(\omega : \vec{k_s}) + N(\omega),$$

where $\vec{v}$ is the array manifold vector, $\vec{k_s}$ is the direction of the signal as a wavenumber, $F(\omega)$ is the source signal of that particular snapshot [93].

The spectral matrix of the noise $N(\omega)$ is

$$S_n(\omega) = S_c + \sigma_\omega^2 I,$$

where σ_ω^2 is the white noise component. For the total signal and noise, $X(\omega)$, the spectral matrix is

$$S_x(\omega) = S_f(\omega) v(\omega : k_s) v^H(\omega : k_s) + S_n(\omega),$$

where $S_f(\omega)$ is the variance of $F(\omega)$ [93].

Without knowledge of the direction of the desired signal and the noise spectral matrix, an optimal beamformer – MPDR – can be derived with the spectral matrix of the signal and noise together, $S_x(\omega)$, by minimizing the output power of the filter with a distortionless constraint [93].

The criteria of a distortionless filter, $\vec{w}^H$, is

$$\vec{w}^H \vec{v_m} = 1,$$

where $\vec{v_m}$ is the steering vector in the direction of the signal [93].

The filter result is

$$\vec{w_{MPDR}}^H = \frac{\vec{v_m}^H S_x^{-1}}{\vec{v_m}^H S_x^{-1} \vec{v_m}} \text{ [93].}$$

In practice, the estimate of S_x changes over time by using the process of time snapshots. As a consequence, S_x is adaptively optimized to the environment which fluctuates over time.

Chapter 5

Experimental Methods

One pool experiment was completed to find the power spectral density of the UUV self-generated noise and two field experiments were completed to demonstrate tracking a UUV in a realistic environment.

5.1 Bluefin Sandshark UUV

The Bluefin Sandshark UUV, pictured in Figure 5-1, was used to demonstrate tracking a UUV in a realistic environment [73].

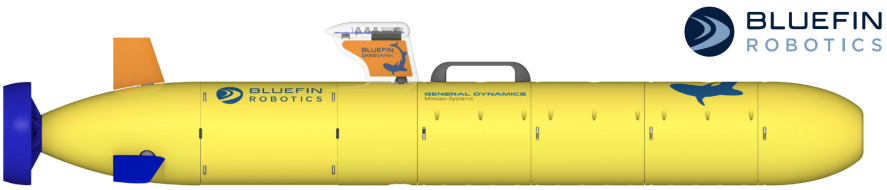

Figure 5-1: Bluefin Sandshark micro-UUV: this micro-UUV manufactured by Bluefin Robotics was used to demonstrate passive detection and tracking in a pond and river experiment [73].

The Bluefin Sandshark is in the micro-size category of UUVs due to its compact size of approximately 15 lbs. The vehicle is torpedo-shaped, with a single propeller. An overview of its manufacturer specifications is in Table 5.1

The estimated position outputted by the inertial navigation system (INS) of the vehicle

Dimensions and Performance	Value	Units
Diameter	12.4	cm
Length	51	cm
Weight	5.12	kg
Depth Rating	200	m
Speed	2 - 4	knots
Power	10	Ah

Table 5.1: Bluefin Sandshark micro-UUV dimensions and performance specifications: the micro-UUV is a man-portable platform and a member of the smallest class of UUVs [73].

was used as the truth measurement for tracking the vehicle in the field experiments. The INS system includes a GPS, IMU, compass, depth sensor, and altimeter. The vehicle software exports a distance, X, Y, that represents its relative distance from the starting position or user-designated origin.

In addition to the standard sensor configuration of the UUV described in the above table, the Sandshark was equipped with a tetrahedral array and was controlled with mission-oriented operating-suite interval-programming (MOOS-IvP) autonomy software.

5.1.1 Tetrahedral Array

The tetrahedral array is on the nose of the vehicle, as pictured in Figure 5-2. The tetrahedral configuration is represented in Figure 5-3. For the purpose of finding the estimate power spectral density (PSD) of the UUV, data was collected on the tetrahedral array, which is a 1 m distance from the main vehicle noise source, the propeller. Although the PSD estimate derived from this pool experiment is consistent with the UUV signature in the pond and river field experiments, the on-board array data could have been subject to shielding from the vehicle hull. The elements of the array are HTI-96-MIN hydrophones, pictured in Figure 5-4 [6]. The hydrophones' signals were converted from analog to digital at a sample rate of 37,500 Hz with the data acquisition device, Measurement Computing USB-1608FS-Plus [14]. The data was then transferred to a Raspberry Pi 3 Model B for storage [9].

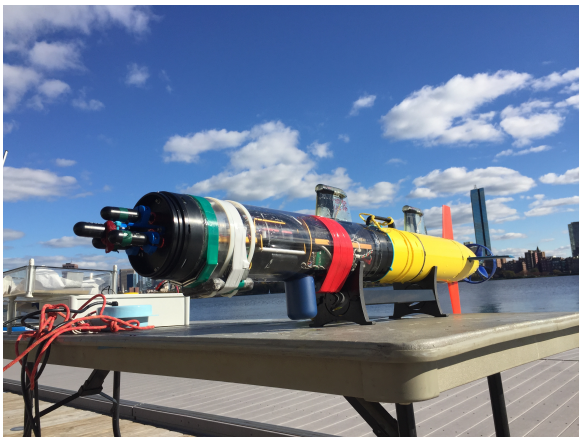

Figure 5-2: Tetrahedral array in nose payload section of the Bluefin Sandshark micro-UUV.

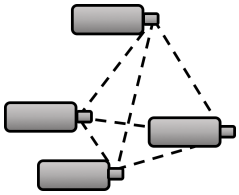

Figure 5-3: Element configuration of a tetrahedral array: a tetrahedral array is in the nose payload section of the micro-UUV, which was used to collect acoustic data for the PSD estimate of the vehicle.

5.1.2 Autonomy – MOOS-IvP

In order for the vehicle to follow a loiter pattern autonomously, MOOS-IvP autonomy software was utilized to control the behavior of the vehicle. MOOS-IvP is open-source autonomous software designed for maritime platforms like UUVs [5]. The software is maintained by MIT and the Oxford Robotics Institute [5].

At a high level, the autonomy decision-making process follows a front seat, back seat configuration [5]. The front seat is defined as the internal vehicle controls and the back seat is run by MOOS-IvP which makes the intelligent autonomous decisions during the mission [5]. The two controllers work together by sharing information [5]. The main vehicle computer sends vehicle state information, including current speed and position [5]. In turn, the autonomy board sends desired speed, heading, and position [5]. This flow of information is represented in Figure 5-5.

Figure 5-4: Hydrophone element HTI-96-MIN: this hydrophone was used to measure the power spectral density estimate of the micro-UUV. Four of the hydrophones are configured in a tetrahedral array in the nose of the Bluefin Sandshark micro-UUV used in these experiments [6].

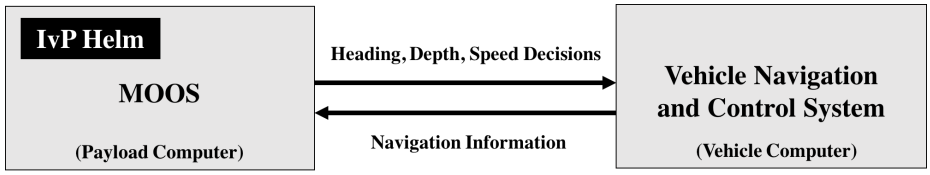

Figure 5-5: Autonomy decision-making process of MOOS-IvP software: MOOS-IvP is configured such that the vehicle computer is separate from the autonomy payload [5].

5.2 Horizontal Line Array

The estimated bearing of the Sandshark UUV was accomplished through beamforming on a horizontal line array. In the experiments, the horizontal line array consisted of six (Charles River) and eight (Jenkins Pond) HTI-96-MIN hydrophone elements [6]. Modeled after the setup in the tetrahedral array, the analog hydrophone signals are converted to a digital signal through the data acquisition system, Measurement Computing USB-1608FS-Plus, at a sampling rate of 19,200 Hz (Jenkins Pond experiment) or 37,500 Hz (Charles River) [14]. Then the data is stored on a Raspberry Pi 3 Model B for future processing [9]. A summary of the transfer of data on the horizontal line array is shown in Figure 5-6.

5.3 Power Spectral Density Estimate – Test Setup

The power spectral density (PSD) experiment with the Sandshark micro-UUV took place at the MIT alumni pool on February 2, 2017. The pool, pictured in Figure 5-7, was chosen for being isolated from outside noise sources. The MIT pool dimensions are 20 ft by 40 ft

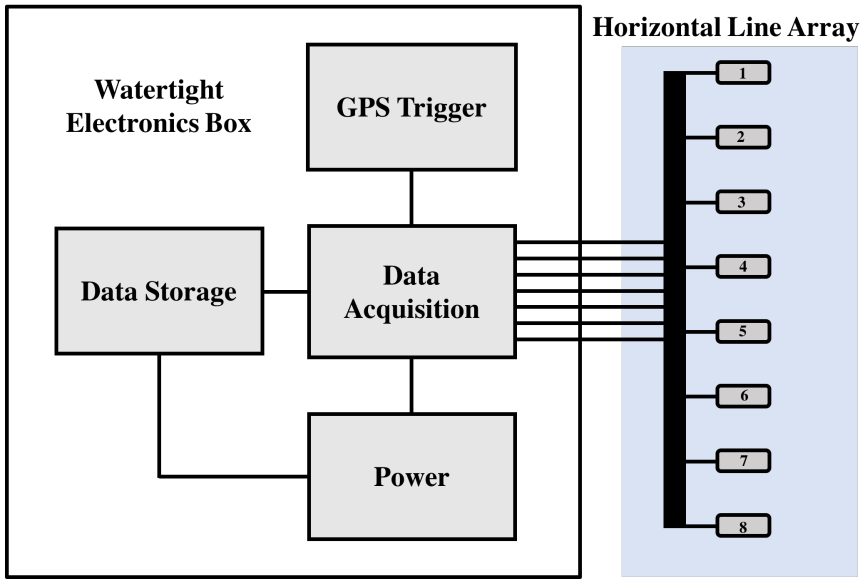

Figure 5-6: Diagram of the horizontal line array and data acquisition setup: data from the horizontal line array was collected using an analog to digital converter, data storage unit, GPS trigger, and power.

by 4 ft.

Representative of a typical vehicle mission, the vehicle speed was approximately 1.5 m/s. The vehicle was held in place while its propeller revolved at the desired speed. During this experiment, the fins were not active. Additional information on the performance and specifications of this UUV are in Section 5.1.

To collect acoustic noise from the propeller, the tetrahedral array in the nose cone was utilized, providing an approximate 1 m (the length of the vehicle) sound level measurement of the propeller noise. The data collection specifications of the array are outline in Section 4.4.2, and the process for deriving the PSD estimate from the array data is described in Section 4.2.

5.4 Jenkins Pond Demonstration – Test Setup

In order to test the possibility of tracking the UUV in a realistic environment, a low-noise test bed was selected: Jenkins pond. A satellite image of the pond is pictured in Figure 5-8.

Jenkins Pond is located in Falmouth, Massachusetts and is approximately 30 ft deep. The experiment, pictured in Figure 5-9, occurred on June 22, 2017.

Figure 5-7: Power spectral density estimate experiment at the MIT alumni pool: the Bluefin Sandshark micro-UUV was secured while its propellor revolved at approximately 1.5 m/s. The onboard acoustic sensors collected acoustic noise data.

The Bluefin Sandshark UUV was used for this experiment and was programmed with MOOS-IvP to follow a loiter behavior. The details of the equipment and autonomy software are in Section 5.1 and Section 5.1.2. Figure 5-10 shows an overview of the vehicle track over time (the colorbar). The vehicle travelled approximately 70 m away from the beach where the horizontal line array was mounted. The depth and speed of the vehicle are shown in Figures 5-11 and 5-12 respectively. The overall vehicle speed was 1.5 m/s while it travelled closely to the surface at 0.5 m depth. This navigation data was produced by the vehicle's inertial navigation system. In post-processing, this data is used as the true position of the vehicle, a benchmark for the estimated bearing from the horizontal line array (HLA). The resurfacing behavior to achieve a GPS fix is shown by the periodic zero-depth and zero-speed of the vehicle.

The HLA was bottom mounted near the starting point of the vehicle at (-40,-60). Data from the array was collected and analyzed post-experiment to derive an estimated bearing and detect the presence of the UUV.

Figure 5-8: Satellite image of Jenkins Pond: array was bottom mounted about 10 m off shore and the vehicle followed a loiter behavior about 100 m off shore.

5.5 Charles River Demonstration – Test Setup

The second demonstration of detecting and tracking a vehicle took place at the Charles River in Cambridge, Massachusetts. This location represented a more cluttered, noisy, and challenging environment to perform the counter-UUV experiment. Figure 5-13 is a birds-eye view of the Charles River bordering the MIT campus.

The MIT sailing pavilion on the river was used as the ground control station. The vehicle was deployed from dock, pictured in Figure 5-14. Throughout the experiment, which was on October 31, 2016, boats passed by the sailing dock producing unwanted, loud acoustic noise. After being deployed, the vehicle proceeded to do a loiter behavior, pictured in Figure 5-15.

The vehicle autonomy was programmed with MOOS-IvP. The vehicle relied on its inertial navigation system for guidance, resurfacing occasionally for a GPS fix.

The periodic zero-depths and zero-speeds shown in Figures 5-16 and 5-17 are representative of the vehicle securing a GPS fix on the surface. The inertial navigation data was used as an estimate of the vehicle's true location to compare to the bearing estimate from the line array. For detecting and tracking the vehicle during its mission, the HLA was secured to the sailing dock. Its exact position corresponds to the origin in Figure 5-15. Therefore, the array was approximately 70 m away from the underway vehicle. A description of the data collection method used in the HLA is in Section 5.2.

Figure 5-9: Shore launch of vehicle at Jenkins pond: the UUV was launched from the shore and the array was bottom mounted about 10 m from the shoreline.

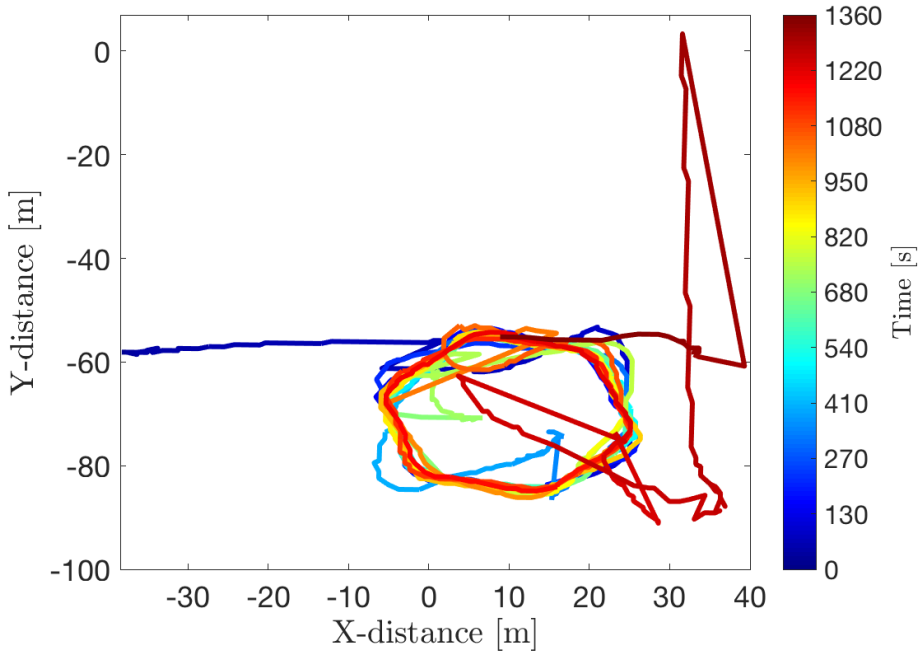

Figure 5-10: UUV track in X-Y coordinates over time at the Jenkins Pond experiment: UUV performed a loiter pattern about 100 m offshore. The progression of time is represented by the colorbar and the total mission time was about 20 min. Navigation data was taken from the vehicle's inertial navigation system.

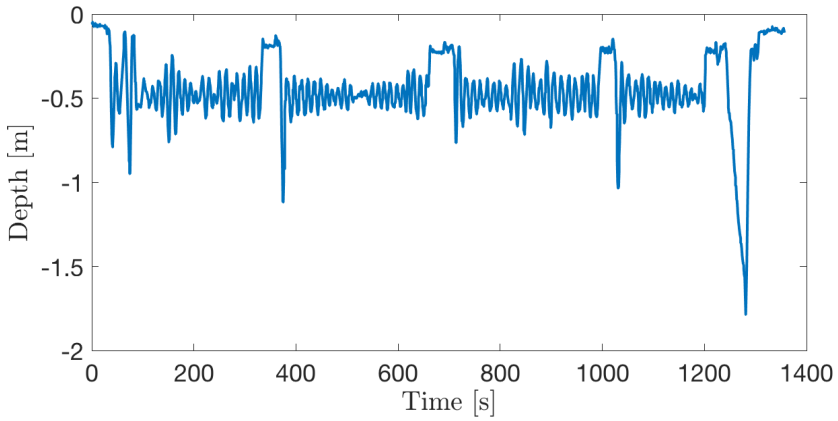

Figure 5-11: UUV depth over time at the Jenkins Pond experiment: depth data was taken from vehicle's inertial navigation system. The short periods of zero-depth are the vehicle surfacing for a GPS fix.

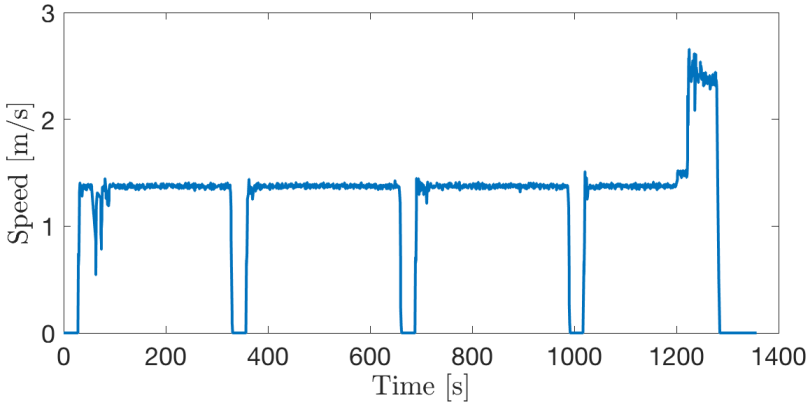

Figure 5-12: UUV speed over time at the Jenkins Pond experiment: speed data was taken from vehicle's inertial navigation system. The short periods of zero-speed are the vehicle surfacing for a GPS fix.

Figure 5-13: Satellite image of the Charles River: the horizontal line array was mounted on the MIT Sailing Pavilion dock and the vehicle followed a loiter behavior about 100 m off shore.

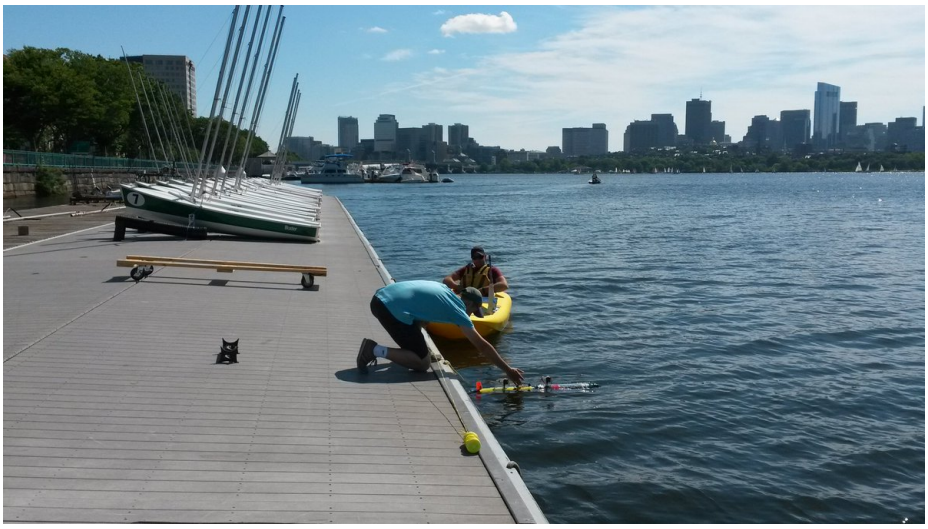

Figure 5-14: UUV was launched from the MIT Sailing Pavilion dock at the Charles River and the array was mounted to the dock.

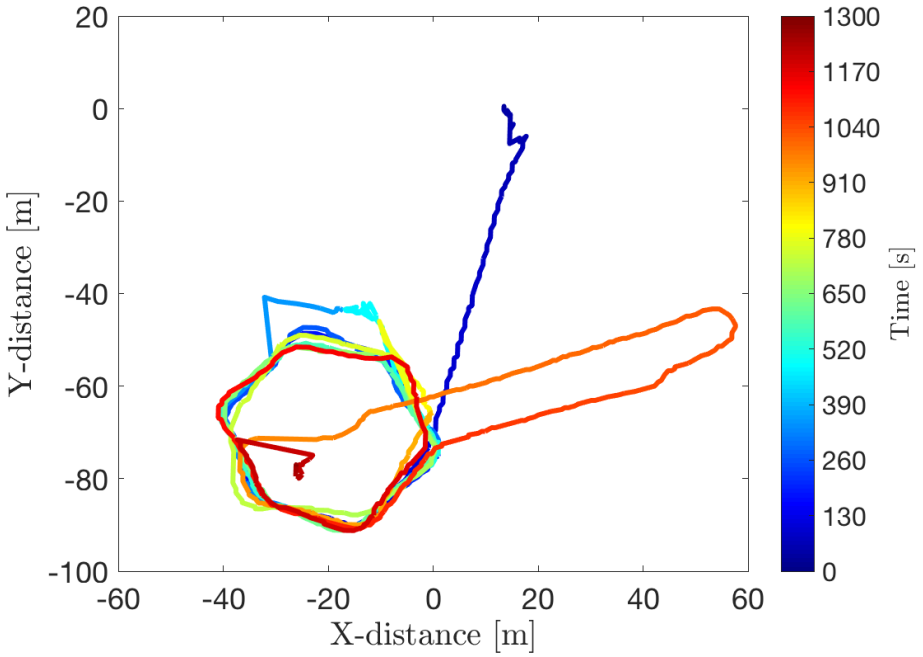

Figure 5-15: UUV track in X-Y coordinates over time at the Charles River experiment: UUV performed a loiter pattern about 100 m offshore. The progression of time is represented by the colorbar and the total mission time was about 20 min. Navigation data was taken from the vehicle's inertial navigation system.

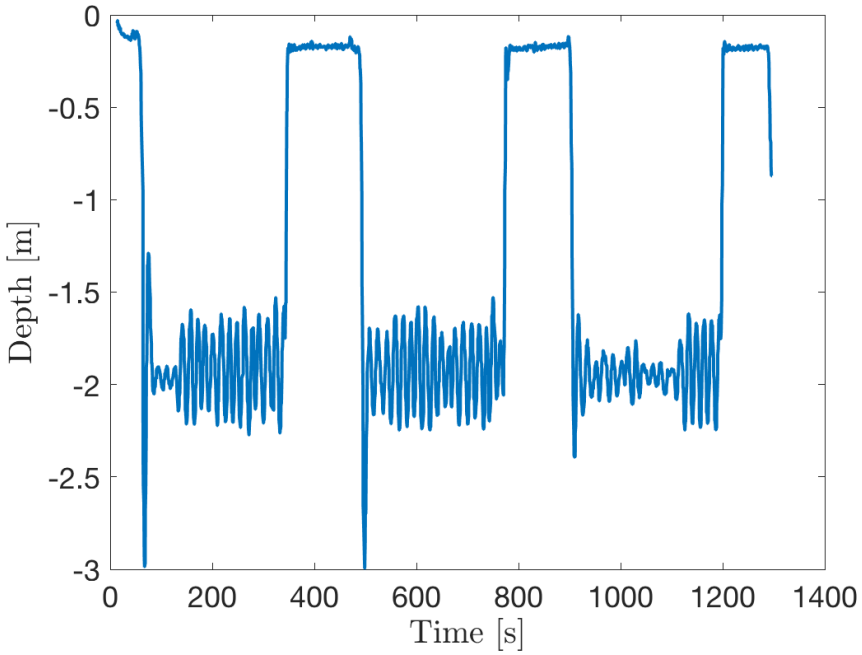

Figure 5-16: UUV depth over time at the Charles River experiment: depth data was taken from vehicle's inertial navigation system. The short periods of zero-depth are the vehicle surfacing for a GPS fix.

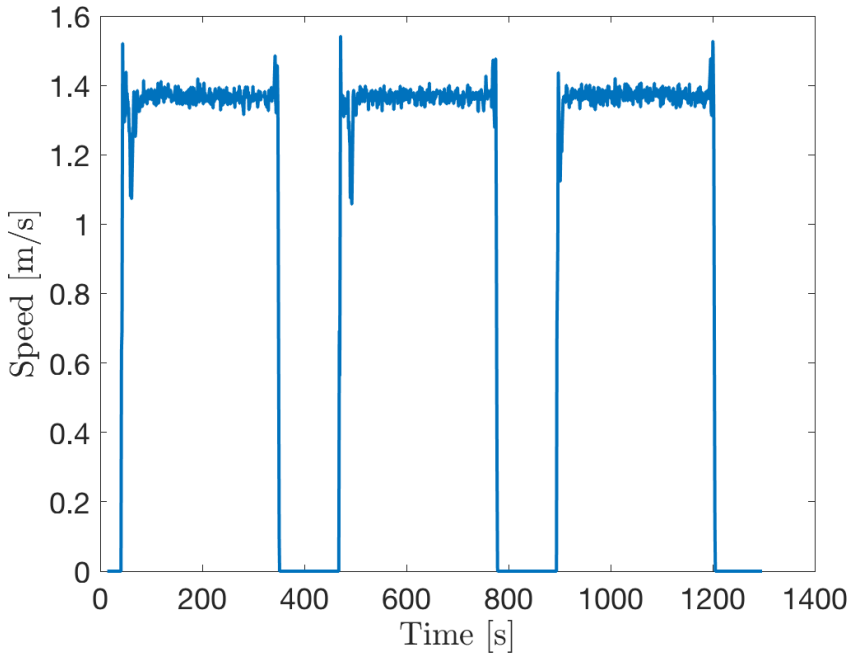

Figure 5-17: UUV speed over time at the Charles River experiment: speed data was taken from vehicle's inertial navigation system. The short periods of zero-speed are the vehicle surfacing for a GPS fix.

Chapter 6

Field Experiments and Results

6.1 Power Spectral Density Estimate – Results

To find the characteristic frequencies of the underway Bluefin Sandshark micro-UUV, a power spectral density estimate in a quiet pool environment was performed on February 2, 2017 at the MIT alumni pool. The experiment is described in detail in Section 5.3. First, a spectrogram, shown in Figure 6-1 of the experiment was generated.

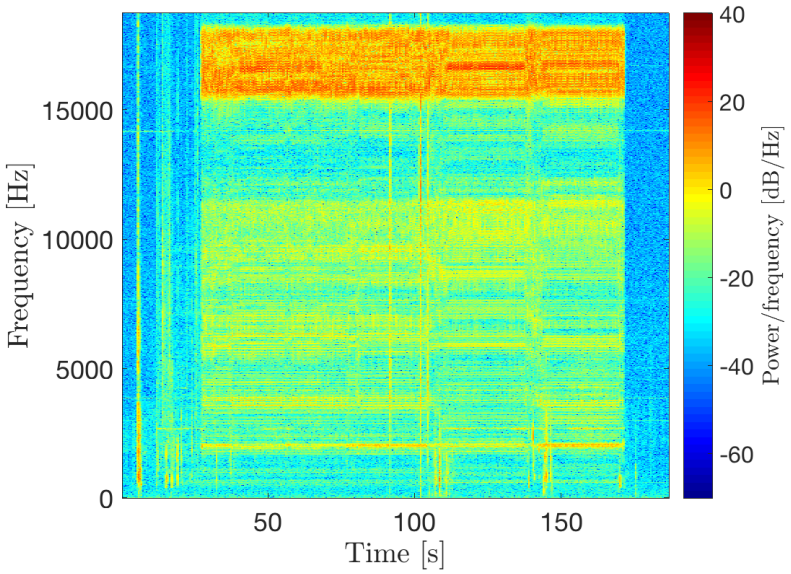

Figure 6-1: Spectrogram of the power spectral density estimate experiment at the MIT alumni pool: the spectrogram shows how frequencies change over time in a visual representation. The vehicle exhibited strong frequencies between 16 kHz and 18 kHz.

This visual representation of the experiment shows the strength of certain frequencies over time. The spectrogram is created by taking the discrete Fourier transform (DFT) of overlapping time segments. The most interesting component of this result is the strong high frequencies of the vehicle between 16 kHz and 18 kHz. For this dataset, however, the sampling frequency, f_s, was 37,500 Hz. As a consequence, the strong frequencies between 16 kHz and 18 kHz were actually aliased, and the true frequency, f_{true}, is between 19,500 Hz and 21,500 Hz:

$$f_{aliased} = |f_{true} - f_s|.$$

This aliasing effect is consistent with the in-water tests of Jenkins Pond and the Charles River.

Secondly, the overall increase in acoustic power at approximately 25 s and 175 s can be observed when the vehicle is turned on and off.

To derive the PSD, the magnitude of each realization, or DFT of the time snapshot, was found, squared, and averaged over all the realizations. The normalized PSD result is in Figure 6-2. The mean and standard deviation are both plotted to show the magnitude of the

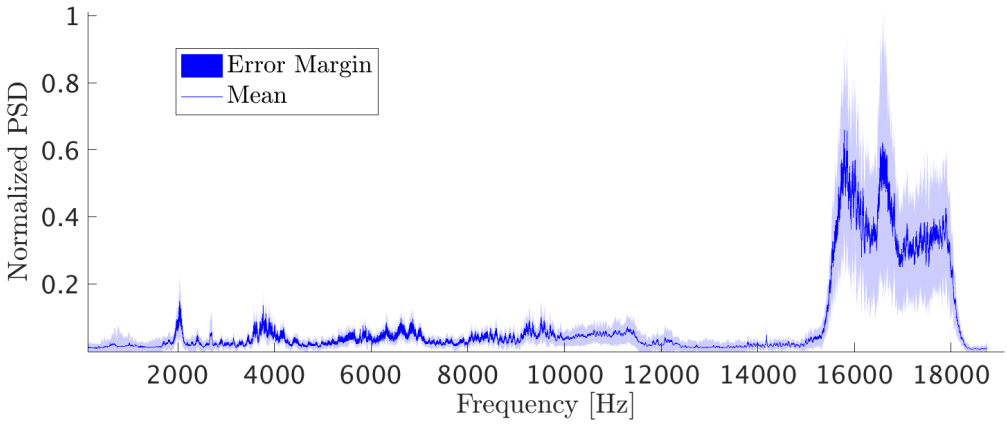

Figure 6-2: Power spectral density estimate of Bluefin Sandshark micro-UUV: the power spectral density estimate was derived from acoustic data collected on-board the vehicle. The data was collected in a pool environment. The standard deviation of the data was used as the error margin.

variance of power over time. This is to be expected because of the random characteristics of broadband propeller noise. Again, as seen in the spectrogram, the high frequencies between 16 kHz and 18 kHz are the most identifying, prominent frequencies of the underway vehicle.

6.2 Jenkins Pond Demonstration – Results

A demonstration of detecting and tracking a vehicle – a Bluefin Sandshark UUV – was performed at Jenkins Pond in Falmouth, Massachusetts, on June 22, 2017. The pond represents an environment that a vehicle might encounter on an ISR mission in littoral waters. The vehicle loitered about 100 m offshore and was picked up and tracked by the bottom mounted array. Section 5.4 describes the array location, vehicle trajectory, and pond dimensions in detail.

The signal from a single hydrophone element was first analyzed by applying short-time Fourier transform and calculating power as a function of frequency. By evaluating the power of different frequency bands, and how they change over time, one can gain knowledge of the environmental noise and vehicle signal. Consequently, the vehicle can be identified in the background noise of the pond – which included foot traffic on the beach, boats passing by, and multipath effects from the shallow water.

In the case of this experiment, the sampling rate was 19,200 Hz and the spectrogram – the frequency power over time – pictured in Figure 6-3 has a cutoff frequency of 9,600 Hz. The vehicle enters the water at about 800 s and is identifiable by its strong frequency around 800 Hz. The vehicle also has strong broadband noise between 3,000 - 4,000 Hz. With the UUV PSD estimate in mind, the vehicle has a strong frequency at 20,000 Hz, which is aliased in the Jenkins pond dataset to 800 Hz.

6.2.1 Detection

Following finding the spectrogram of the experiment, energy across the frequencies was calculated to detect the presence of the vehicle. To improve detection, a bandpass filter was also used on the 800 Hz, the aliased but identifiable, frequency of the vehicle.

Figure 6-4 is the ROC curve comparison of filter applied and no filter. With no filter, the probability of detection is 70.4 % and probability of false alarms is 49.4 %. With a bandpass filter on the aliased frequency of 800 Hz, this improves to a probability of detection of 71.0 % and false alarm rate of 36.0 %. False alarms decreased by 13.5 %.

The ROC curve area, presented in Figure 6-5, is a measure of how well the detector performs. In the case of no filter, the area was 0.61, which is close to 0.5, so it is considered a very poor detector – 50 % false alarms, 50 % true detection. By adding a bandpass filter

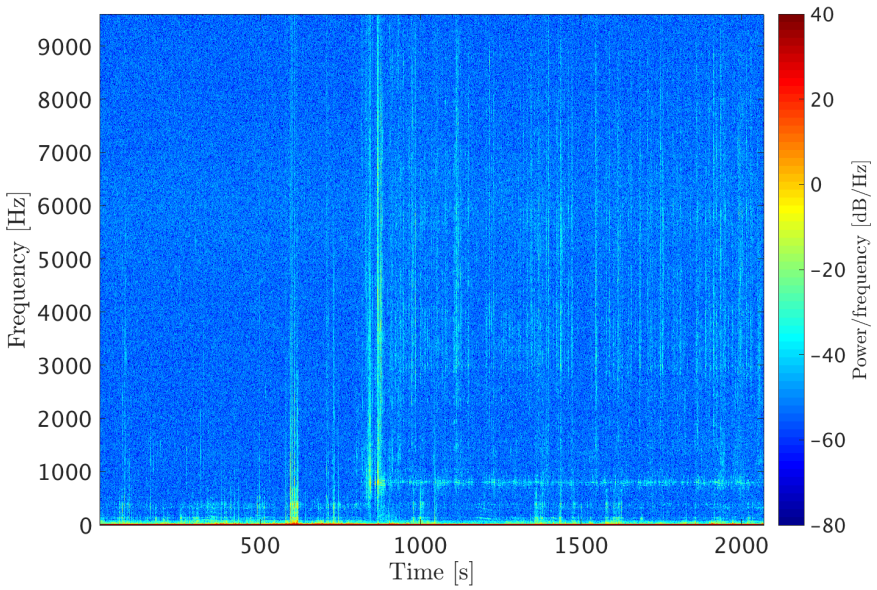

Figure 6-3: Spectrogram of the Jenkins Pond experiment: the spectrogram shows how frequencies change over time in a visual representation. The vehicle is identifiable by its strong frequency tone at 800 Hz, which is aliased down from the true frequency of 20 kHz. The vehicle enters the water at around 800 s.

the area increases to 0.69.

The detection results are compared in Table 6.1, which shows that the filter decreases the false alarms rates by 13.5 %.

	No Filter	Bandpass Filter
P(D)	70.4	71.0
P(FA)	49.5	36.0

Table 6.1: Probability of detection and false alarms from the ideal detection threshold for the Jenkins Pond experiment. The bandpass filter was applied to the aliased frequency of 800 Hz.

6.2.2 Tracking

After confirming the presence of the vehicle, in practice, the bearing of the vehicle is tracked over time – giving insight to the vehicle's true trajectory and intentions.

In the Jenkins Pond experiment, the vehicle bearing is estimated with a horizontal line array with specifications outlined in Section 4.4.2. The array was bottom mounted and about 80 m from the vehicle while it followed a loiter pattern.

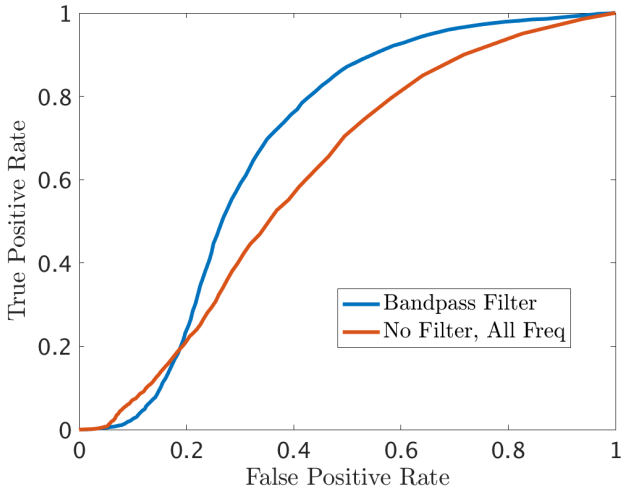

Figure 6-4: ROC curves from the Jenkins Pond experiment: the bandpass filter applied to the aliased frequency of 800 Hz outperforms no filter applied to the data.

Since the vehicle changed direction over time, the array data was divided into time snapshots, then DFT and beamforming was carried out on each segment. These results, with conventional beamforming, are in Figure 6-6. The x-axis is time, showing how the beamforming results evolve. At each time segment, the beamforming results were averaged over frequencies, 1000 - 8000 Hz, because of the broadband nature of the vehicle. There is a broadband interferer at broadside or 90 °. This is potentially due to interference on the beach – like people and boat traffic. Despite this intense interferer, the triangular trajectory that oscillates between 80 ° and 120 ° is the true trajectory of the vehicle.

In Figure 6-7, the expected true trajectory of the vehicle is plotted in blue. This was found using the inertial navigation system and the orientation of the array. The beamforming results, plotted in red in Figure 6-7, follow the same shape – a triangular function over time – which correlates to the vehicle pursuing a loiter pattern.

Due to the interferer at broadside, the maximum beamforming results match the shape but not the exact troughs and peaks of the true trajectory. The expected vehicle bearing, calculated from the vehicle inertial navigation system, is between 80 ° and 115 °; instead the estimated bearing, from the array data, is between 90 ° and 105 °. The maximum beamforming results were found by applying a smoothing filter to the maximum beamformer output described in Section 4.4.4.

For a comparison over time, Figure 6-8 shows the absolute angle difference between

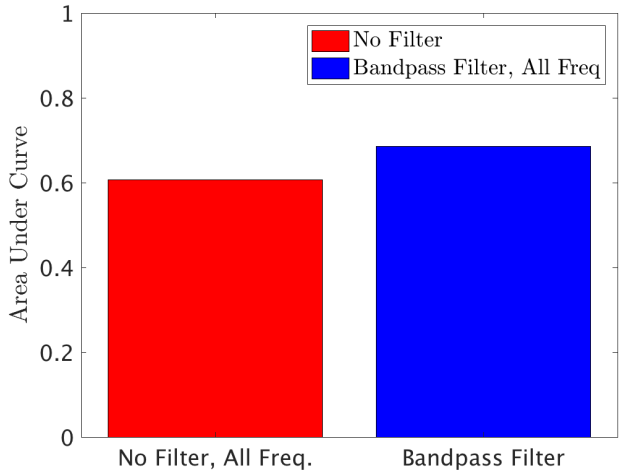

Figure 6-5: Area under the ROC curves of the Jenkins Pond experiment: the area under the curve is a measure of the ROC curve performance. The bandpass filter increases the area under the curve by about 10 %.

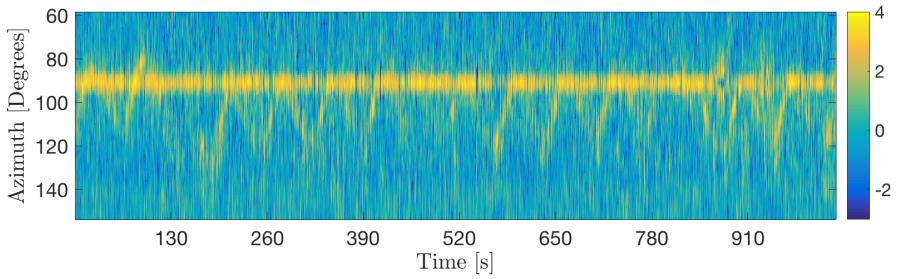

Figure 6-6: Conventional beamforming results of the Jenkins Pond experiment: the true vehicle track is the triangular pattern shown in the beamformer. There is a broadband interferer at 90 °.

the estimated and true trajectory. Better results would be expected without the interferer; however, the average error was only 7.4 ° with a standard deviation of 5.2 °. This was calculated over the time window of 380 s to 675 s.

In addition to conventional beamforming, MPDR was applied to the dataset to minimize background noise, pictured in Figure 6-9.

In order to use an MPDR filter in an environment that changes with time, the spectral matrix of the array was calculated and averaged over individual time segments. This adaptive beamformer strategy is recounted in detail in Section 4.4.5.

The MPDR results slightly outperformed the conventional beamformer. Comparing the same time period as the conventional beamformer results, the average error was only 7.0 °

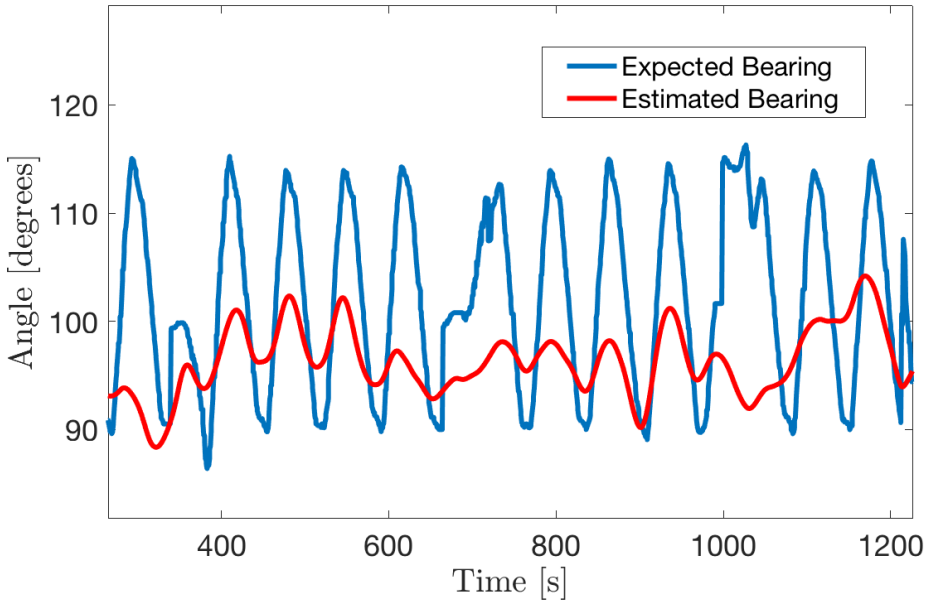

Figure 6-7: Estimated versus expected bearing of the UUV at the Jenkins Pond experiment with conventional beamforming.

with a standard deviation of 4.5°. A comparison of the true vehicle track (blue) and the beamformer estimated bearing (red) is plotted in Figure 6-10. The absolute angle difference, or error, between the estimated and expected bearing is shown in Figure 6-11.

In comparison, MPDR slightly decreased the mean and standard deviation by approximately 0.5°, which is summarized in Table 6.2.

	Error (Absolute angle difference)
Conventional	$7.4 \pm 5.2\,^\circ$
MPDR	$7.0 \pm 4.5^\circ$

Table 6.2: Comparison of absolute angle difference, or error, between conventional and MPDR beamforming at the Jenkins Pond experiment

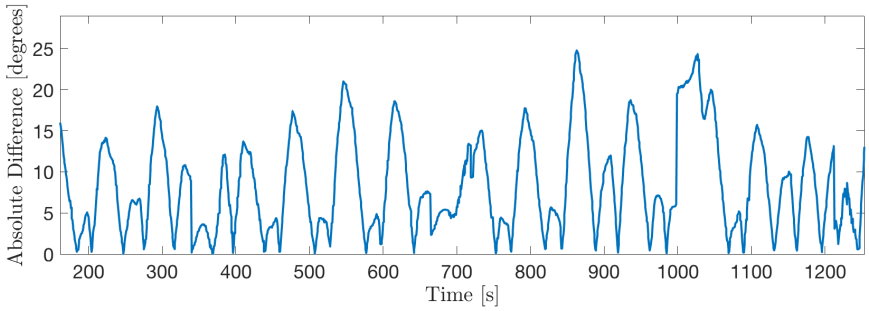

Figure 6-8: Absolute difference, or error, between the estimated and expected bearing of the vehicle over time at the Jenkins Pond experiment with conventional beamforming

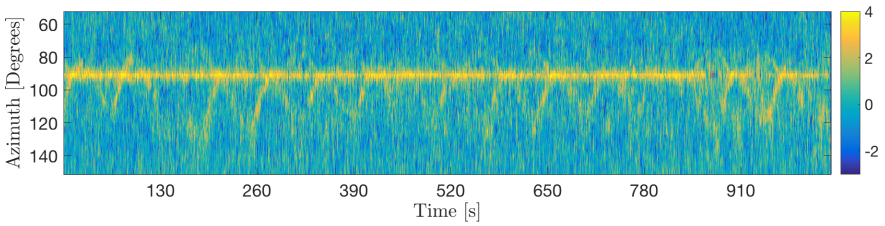

Figure 6-9: MPDR beamforming results of Jenkins Pond experiment: the vehicle true vehicle track is the triangular pattern shown in the beamformer. There is a broadband interferer at 90 °.

6.3 Charles River Demonstration – Results

The Charles River lies between Cambridge and Boston, Massachusetts. During the day, boats of various kinds, frequent the river, offering a dynamic acoustic environment that would be able to test the limits of detecting and tracking a UUV with a high level of background noise across all frequencies. This situation is on par with the background noise of a UUV navigating a harbor environment for deploying sensors or ISR.

The MIT sailing pavilion, which is on the Cambridge side of the river, was the ground control station for the experiment. Additional information on the experiment is laid out in detail in Section 5.5.

For a preliminary assessment of the vehicle and environmental noise, a spectrogram was generated from a single hydrophone element. The spectrogram, which is in Figure 6-12, shows the progression of strong frequencies over time. The x-axis is time, the y-axis is frequency, and the color is the power level in decibels. Putting it all together, the spectrogram reveals what frequencies are stronger than others and how they change over

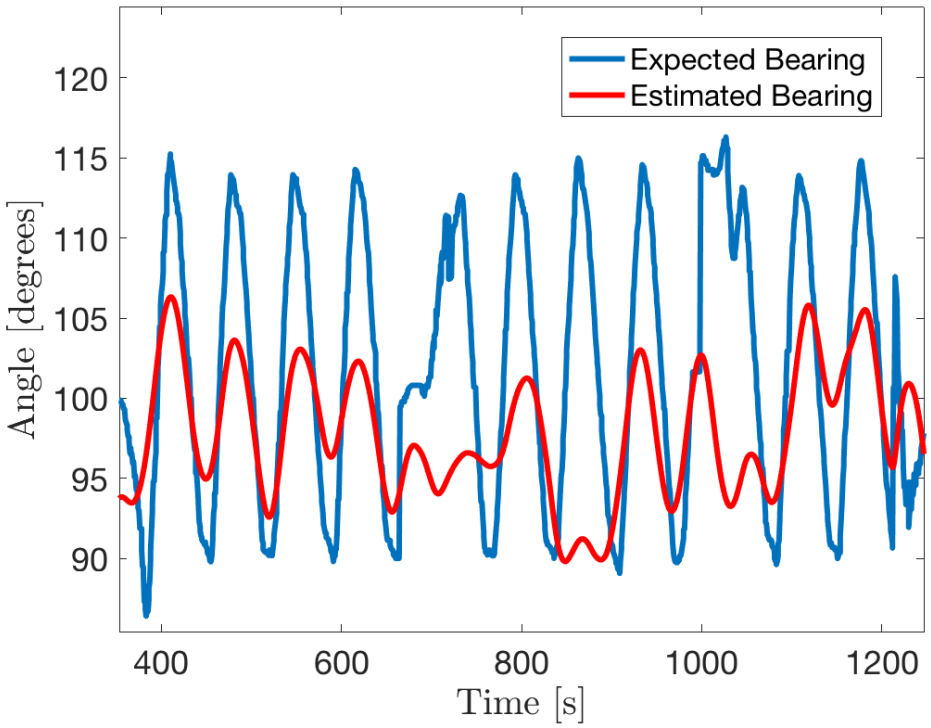

Figure 6-10: Estimated versus expected bearing of the UUV at the Jenkins Pond experiment with MPDR beamforming.

time. This spectrogram was created using a 50% overlap of time segments and a sampling frequency of 37,500 Hz.

The vehicle enters the scene at about 300 s and exits at 800 s. The vehicle is identifiable by a strong tone at 17,500 Hz which is actually an aliased frequency of 20 kHz. The vehicle noise is also apparent by its broadband noise from 2,000 Hz to 8,000 Hz.

The broadband short bursts at 50 - 70 s and 650 - 700 s are examples of a boat passing by. The strong tone that fluctuates between 10 kHz and 12 kHz was present in the entire dataset. Its origin is unknown, but it could be caused by a loud electronics source on the boat dock.

6.3.1 Detection

After observing the spectrogram features of the data, detection analysis was performed by energy thresholding and spectral filtering to detect the vehicle in background noise. The three filters applied were the power spectral density (PSD) estimate as a filter, across all

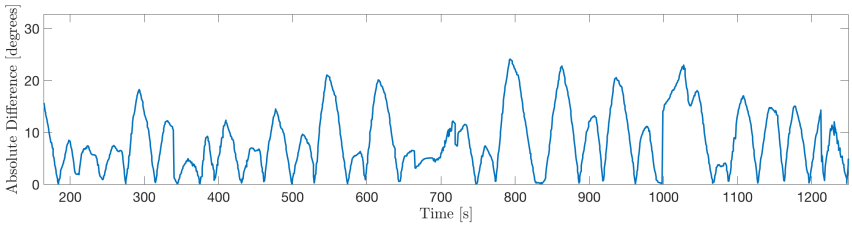

Figure 6-11: Absolute difference, or error, between the estimated and expected bearing of the vehicle over time at the Jenkins Pond experiment with MPDR beamforming.

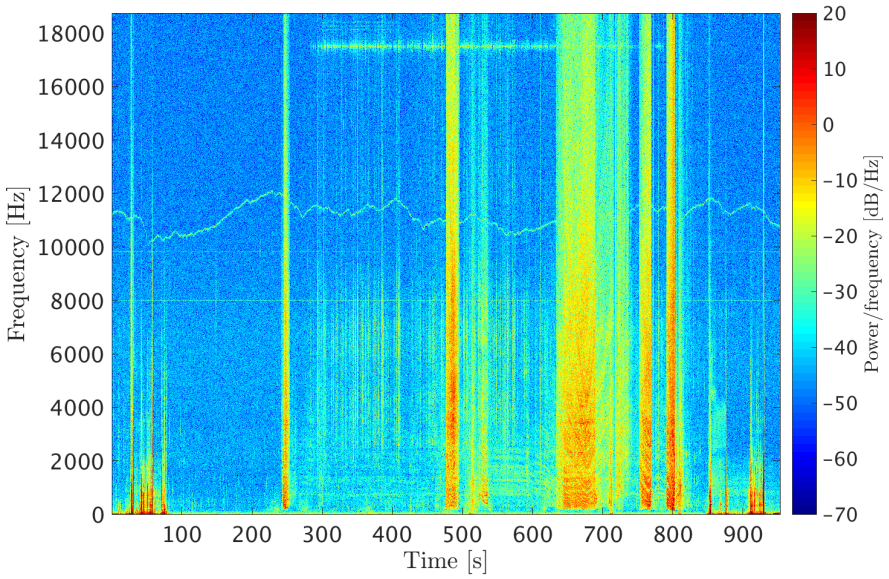

Figure 6-12: Spectrogram of the Charles River experiment: the spectrogram shows how frequencies change over time in a visual representation. The vehicle is identifiable by its strong frequency tone at 17500 Hz, which is aliased down from the true frequency of 20 kHz. The vehicle enters the water at around 300 s.

frequencies; a bandpass filter from 16 kHz to 18 kHz; and finally a combination of both, the PSD as a filter and the bandpass filter from 16 kHz to 18 kHz.

The frequency filter specifications were derived from the PSD results from the pool test outlined in Section 4.3.3. The purpose of comparing the different filters is to see how much the probability of detection, $P(D)$, increases and the probability of false alarms, $P(FA)$, decreases if knowledge of the UUV spectral signature is available. These results, presented in Figure 6-13 as ROC curves, quantify the advantage of using spectral filters on the data. The ROC curves were created by doing STFT on the data, applying the filters, calculating energy, and setting different detection thresholds. This process is discussed in Section 4.3.

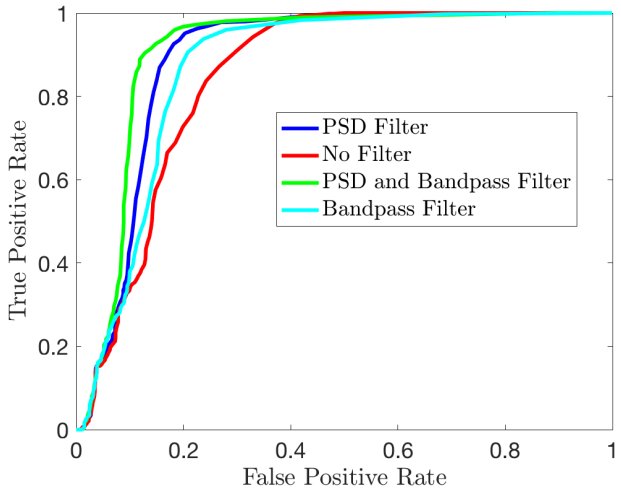

Figure 6-13: ROC curves from the Charles River experiment: three different filters were applied to the dataset to increase the SNR of the vehicle signature. The first filter was a bandpass filter from 16 kHz to 18 kHz. The second filter was the PSD estimate as a frequency shaping filter. Finally, the third filter was a combination of the bandpass filter and the PSD filter. The combination of the bandpass filter and PSD filter outperformed the other spectral filters. No filter applied, represented in red, performed the worst.

On the ROC curve plot, red represents energy detection with no filter applied; unsurprisingly, it performs the worst. The green line, the PSD and bandpass filter together, has the best true positive rate versus false alarms, followed by the PSD as a filter in the dark blue. To quantify the performance of the ROC curves, the area under the curves was found and displayed in Figure 6-14. As discussed in the theory behind ROC curves, the ideal area under the curve is one for perfect detection and no false alarms. The ideal detection thresholds were calculated for each case and summarized in Table 6.3.

	No Filter	Bandpass Filter	PSD	Bandpass Filter and PSD
P(D)	97.5	93.8	95.1	95.9
P(FA)	37.0	23.8	20.3	18.3

Table 6.3: Probability of detection and false alarms from the ideal detection threshold for the Charles River experiment. The bandpass and PSD filter combination had the best performance.

The PSD and bandpass filter outdid the base case of no filtering by decreasing the probability of false alarms by 18.8%.

These probabilities were calculated over the entire dataset, which included boats passing

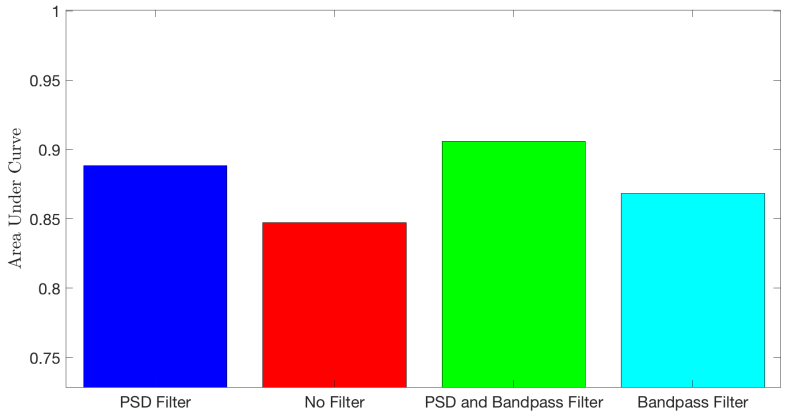

Figure 6-14: Area under the ROC curves of the Charles River experiment: the area under the curve is a measure of the ROC curve performance. The PSD and bandpass filter combination increases the area under the curve by about 10% from no filter applied

by. In the case of a harbor with little activity, it is expected that these detection rates would be even better. Furthermore, it should be noted that this and the previous experiments were conducted with the Sandshark micro-UUV, which is the smallest class of vehicles. As vehicles increase their size, the potential number of sources of electro-mechanical noise also increases – such as the complexity and size of the propulsion system. The detection results have the potential to improve on mid- to large-sized vehicles that are more commonly used by navies.

6.3.2 Tracking

Succeeding the detection of the UUV with energy thresholding and spectral filtering, the vehicle noise source was tracked with a horizontal line array. The array provides an estimate bearing to the vehicle position which, in practice, could provide situational awareness of a UUV's intent to a ship, harbor, or submarine.

In the Charles River experiment, the horizontal line array (HLA) was mounted to the sailing pavilion dock where the vehicle was initially deployed. Pictures of the setup are provided in Section 5.5.

The HLA consisted of six elements with a spacing of 0.075 m and a temporal sampling frequency of 37,500 Hz. As outlined in Section 4.4.4, the array data was segmented into overlapping time snapshots. Then DFT was applied and this result was beamformed, and

later averaged across frequencies, 1000 Hz to 8000 Hz. The beamformer results are presented in Figure 6-15. The maximum beamformer result, seen in Figure 6-16, was extrapolated and

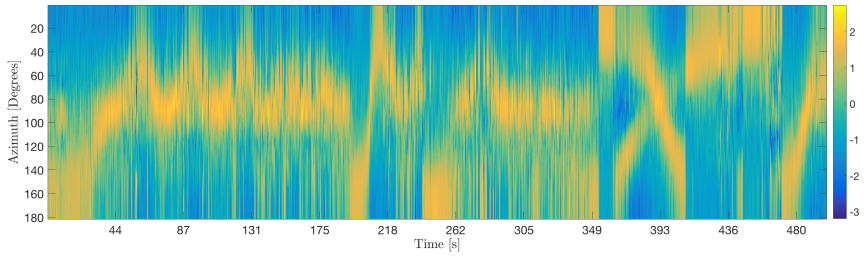

Figure 6-15: Conventional beamforming results of the Charles River experiment: the true vehicle track is the triangular pattern shown in the beamformer.

smoothed with a procedure discussed in Section 4.4.4. When a boat enters the scene, its

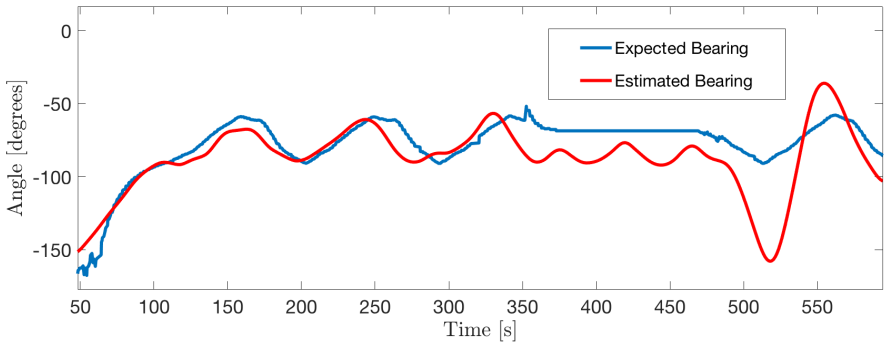

Figure 6-16: Estimated versus expected bearing of the UUV at the Charles River experiment with conventional beamforming.

bearing estimate is also tracked by the HLA. As a demonstration of this effect, in Figure 6-15, the track splits in two from 350 s to 400 s. In the experiment, the vehicle completed a loiter pattern which appears as a triangular pattern over time. The shape of this trajectory is depicted in Figure 6-15.

To evaluate the performance of the beamformer, the true vehicle bearing with respect to the array orientation was found using the data from the vehicle inertial navigation system. Both of these tracks are plotted in Figure 6-16 for the portion of data without boat interference. The bearing estimate was, on average and without boat interference, 10.5 ° different from the true track. This bearing error had a standard deviation of 7.1 ° and is plotted as the absolute difference over time in Figure 6-17.

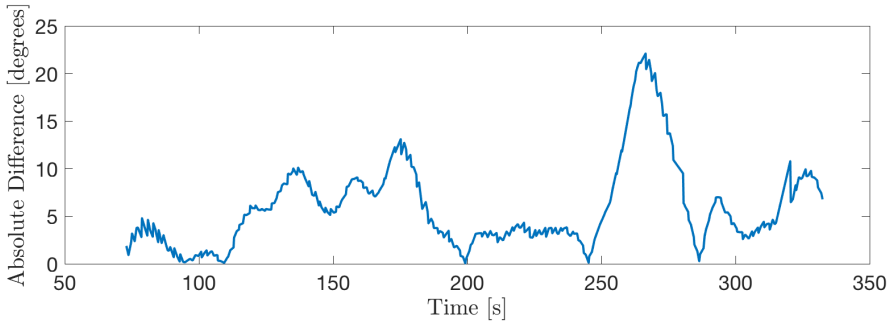

Figure 6-17: Absolute difference, or error, between the estimated and expected bearing of the vehicle over time at the Charles River experiment with conventional beamforming

As a follow-on to conventional beamforming, MPDR was applied to improve the SNR of the vehicle signature during beamforming. The MPDR filter was adaptive to the environment since the spectral matrix of the array was recalculated over time. The technical procedure of applying this filter is described in Section 4.4.5. Figure 6-18 shows the beamforming results after using MPDR. Visually, the triangular bearing estimate of the vehicle

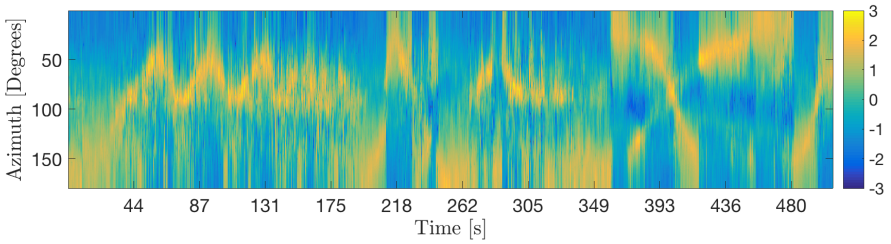

Figure 6-18: MPDR beamforming results of Charles River experiment: the true vehicle track is the triangular pattern shown in the beamformer.

is more defined, narrower, and cleaner than the conventional beamformer results. In one section of the data, from approximate time 350 s to 400 s, the MPDR cancels out the boat trajectory.

Considering the same time segment as the conventional beamformer results, the maximum beamformer results are plotted against the true vehicle track in Figure 6-19. The average angle difference, or error was 6.2 ° with a standard deviation of 5.7 °. The absolute difference over time is presented in Figure 6-20. It shows that at certain points, the MPDR beamformer filter is less than 5 ° away from the true track.

In contrast to the conventional beamformer, the MPDR filter decreased the mean error by 4 °. These results are presented and compared in Table 6.4.

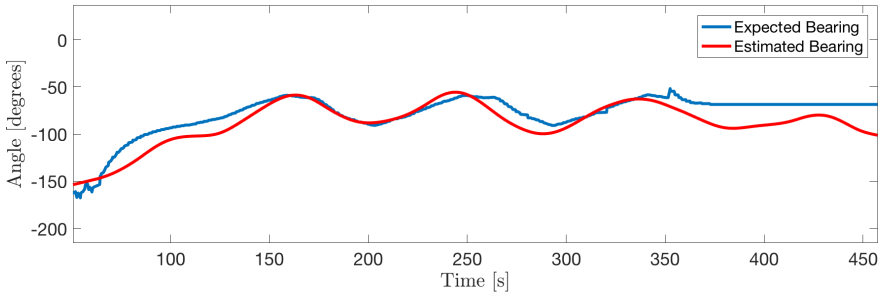

Figure 6-19: Estimated versus expected bearing of the UUV at the Charles River experiment with MPDR beamforming.

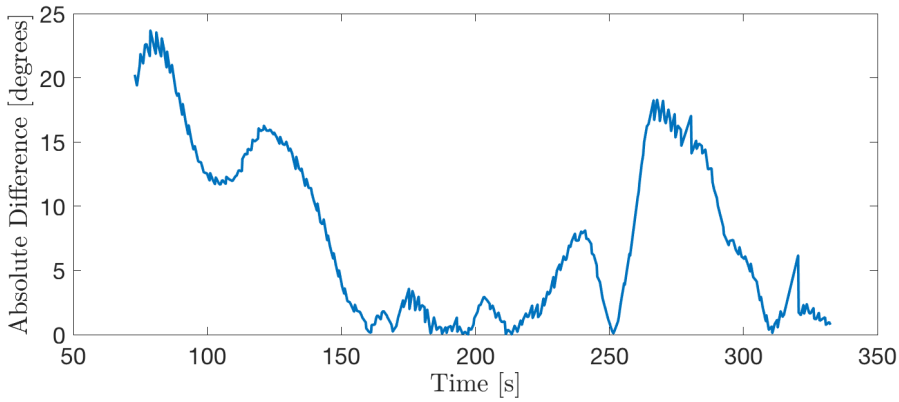

Figure 6-20: Absolute difference, or error, between the estimated and expected bearing of the vehicle over time at the Charles River experiment with MPDR beamforming.

	Error (Absolute angle difference)
Conventional	$10.6 \pm 7.1\,^{\circ}$
MPDR	$6.2 \pm 5.7^{\circ}$

Table 6.4: Comparison of absolute angle difference, or error, between conventional and MPDR beamforming at the Charles River experiment.

For future investigation, the line array could be optimized for the most distinctive frequencies of the vehicle – around 20 kHz. MPDR would have an even greater effect in eliminating unwanted background noise.

Chapter 7

Conclusion

The role of UUVs has evolved from mapping and MCM to advanced missions of tracking plumes [79] and under ice exploration [19]. Technology has enabled these complex missions, specifically by advancing small-SWAP sensors to improve navigation, autonomy to make decisions without a human operator in a highly dynamic, unpredictable environment, and energy to go long distances without refueling.

However, improved UUV capabilities have led UUVs to play a role in asymmetric warfare. Countries with less-established navies can even the playing field by leveraging UUVs: UUVs are low-cost, easy to deploy, covert, difficult to detect, act as force-multipliers, and reduce the risk to personnel because they are autonomous.

As a result, the U.S. Department of Defense has a prime interest in investing in counter-UUV technology. For example, DARPA has published a BAA for "Open Ocean Counter Unmanned Underwater Vehicle (OOCUUV) Study" [30], Strategic Systems Program for Nuclear Weapons Security has called for small business innovation research (SBIR) for "Unmanned Undersea Vehicle (UUV) Detection and Classification in Harbor Environments" [4], and the U.S. Department of the Navy has requested a "Counter-Unmanned Undersea Vehicle (C-UUV) Capability Demonstration for the Stiletto Maritime Demonstration Program" [2].

This thesis is a response to this growing need – to create technology to covertly detect and track UUVs with confidence and protect ships, harbors, and submarines from UUVs of malicious intent. The solution discussed in this thesis could also be integrated into existing passive acoustic surveillance systems.

The significant contributions of this thesis are:

1. Analysis of the frequency spectrum of a micro-UUV's self-generated noise

2. Field experiments in a pond and river quantifying the detection and false alarm rates of a UUV with different spectral filters

3. Field experiments in a pond and river demonstrating tracking a UUV using conventional and adaptive beamforming on a horizontal line array.

This work addresses a key element to the counter-UUV problem: how confidently can a UUV be recognized and tracked in a realistic ocean environment?

This thesis starts with an overview of what UUVs are and how they are used. Each electro-mechanical subsystem is described in detail in Section 2.1, emphasizing what causes unwanted acoustic noise that is used to detect and track the vehicle in the experiments. This chapter also highlights the common ground of UUV design. Most vehicles, like the Sandshark micro-UUV used in this thesis, have a torpedo-shaped hull and single propeller propulsion system. Larger vehicles are more prevalent in the U.S. Navy and it can be expected that these mid- to large-sized vehicles have a louder, more detectable acoustic signature. With a more complex electro-mechanical system and additional sensors, the overall acoustic noise will increase and the probability of detection is likely to be better for these vehicles than that of the micro-UUV used in this thesis.

Following the motivation and background of UUVs and counter-UUV technology, the third chapter provides an overview of existing research in UUV acoustic spectral analysis, and acoustic passive detection and tracking of maritime platforms. Although passive acoustics are widely used for ships and submarines, this thesis is one of the first demonstrations of applying these methods to UUVs.

The theory behind detecting and tracking is outlined in the fourth chapter. Then the fifth chapter explains the hardware specifications and field test setups to validate and quantify tracking the vehicle in a pond and river.

Finally, the sixth chapter presents the results of the individual experiments: the estimated PSD, and two demonstrations of detecting and tracking the Sandshark micro-UUV in a pond and river. The purpose of estimating the PSD of the vehicle was to understand the identifying spectral features of the vehicle while it was underway, how the features changed

over time, and to derive the spectral filters for energy detection. This was accomplished by measuring the acoustic noise from the vehicle in a pool environment. The vehicle revealed a PSD that had a standard deviation of about 20 %. The fluctuation in the PSD, represented as a standard deviation or error, is not surprising, given that the propeller acoustic energy is broadband and random. The vehicle also exhibited strong, high-frequency tones between 16 kHz and 18 kHz, which were actually aliased from the true frequency of about 20 kHz.

With information from the PSD estimate, different spectral filters were applied to the acoustic data collected in the pond and river experiments to increase the true detection rate of the UUV. ROC curves were produced to find the optimal energy detection threshold. The highest performing filter was the combination of the PSD filter (as a frequency shaping filter) with the bandpass filter from 16 kHz to 18 kHz. For the two in-water experiments, realistic inference occurred, like boats passing by.

For the Jenkins Pond experiment, the tracking and detection results yielded worse performance than the Charles River experiment for two reasons. First, a broadband interferer disrupted the beamforming results. Secondly, the strong tone of the vehicle of 20 kHz was aliased down to 800 Hz instead of 17.5 kHz, as in the Charles River experiment. In the lower frequency range, there is more background noise. Despite these shortcomings, the bandpass filter on 800 Hz decreased the probability of false alarms from 49.5 % to 36.0 %. The beamformer results were within 7.4 degrees of the true track for conventional beamforming and 5.2 degrees for MPDR.

The Charles River case, on the other hand, had the same sampling rate as the data acquisition system used to derive the PSD estimate. Therefore, the PSD could be used as a filter on the Charles River data, increasing the frequencies of importance. The other filter applied to the Charles River dataset was a bandpass filter on the 16 kHz to 18 kHz range. The combination of the two filters performed the best, resulting in a probability of detection of 96.0% and probability of false alarms of 18.3% which, compared to no filter, decreased false alarms by 18.8%. The beamformer output produced 10.6 degrees within the true track of the vehicle and 6.2 degrees for the beamformer with MPDR.

In order to improve upon these results, additional analysis of the causes of the acoustic PSD of the vehicle is recommended. The PSD estimate test should also be repeated with acoustic sensors off-board the vehicle to remove the possibility of shielding. The detection and tracking experiments could be repeated with higher sampling rates to prevent aliasing

the identifiable high frequency tones. In addition, more UUV types can be investigated – particularly larger vehicles which are more commonly used – to confirm the hypothesis that they have a similarly shaped PSD estimate but overall louder signature.

For future field tests, interferers like the broadband noise found in Jenkins Pond, and more generally, boats passing by, should be analyzed to prevent false alarms and improve the beamformer output. By understanding the environmental noise, predicting the confidence level or ideal threshold can be found for more scenarios. As noted in the Section 4.3.4, energy thresholding is highly dependent on the background noise levels.

Since the UUV showed strong high frequency tones while underway, the acoustic horizontal line array (HLA) should be optimized with this in mind. The next iteration of the HLA should be equipped spatially and temporally to track a 20 kHz signal that is emitted by the vehicle.

To take the experiment a step further, one should consider different environments like open ocean and multi-vehicle tracking experiments. Furthermore, tracking UUVs on-board moving platforms such as submarines, ships, and other UUVs is of interest, particularly in areas of the ocean where a bottom-mounted array isn't feasible, available, or practical. On the processing side, a predictive model using the dynamics of the UUV could be incorporated into estimating the global track of the vehicle. An example of target motion analysis is using a Kalman filter. Lastly, acoustic propagation models could be leveraged to test the performance of the detection algorithm under different conditions. The PSD estimate of the vehicle could be used as input to the model.

With the rapid improvement of technology in UUVs, the list of possible scenarios to test and prepare for against UUVs of malicious intent is constantly being added to. The core issue of the counter-UUV problem is unchanged, however: to confidently and covertly detect and track UUVs to understand their intent. With two demonstrations in realistic environments, this thesis shows that, indeed, despite the challenges of countering UUVs, they can be found and tracked with identifiable spectral features. The findings of this thesis contribute one step forward in security technology to protect against the potential threat of UUVs to harbors, ships, and submarines.

Bibliography

[1] Bluefin Robotics. http://www.versusrisk.com/en/bluefin-robotics/.

[2] Counter-Unmanned Undersea Vehicle (C-UUV) Hosted by the Stiletto Maritime Demonstration Program. Technical report, ASD Rapid Reaction Technology Office, Stiletto Maritime Demonstration Platform.

[3] Curve Fit: Smooth response data. https://www.mathworks.com/help/curvefit/smooth.html.

[4] Department of the Navy (DoN) 15.2 Small Business Innovation Research (SBIR) Proposal Submission Instructions. Technical report, Office of Naval Research (ONR).

[5] Design Considerations of MOOS-IvP. https://oceanai.mit.edu/ivpman/pmwiki/pmwiki.php?n=Helm.HelmDesignIntro.

[6] HTI-96-Min Hydrophone Series. http://www.hightechincusa.com/products/hydrophones/hti96min.html.

[7] HYbrid Coordinate Ocean Model (HYCOM). https://hycom.org/.

[8] One ROC Curve and Cutoff Analysis. Technical report, NCSS Statistical Software.

[9] Raspberry Pi 3 Model B- Specifications. https://www.raspberrypi.org/products/raspberry-pi-3-model-b/.

[10] REMUS and Mine Countermeasures. https://www.onr.navy.mil/en/About-ONR/History/tales-of-discovery/remus.

[11] Trapezoidal numerical integration. https://www.mathworks.com/help/matlab/ref/trapz.html.

[12] A Survey of Missions for Unmanned Undersea Vehicle. Technical report, RAND Corporation, Santa Monica, 2009.

[13] U.S. underwater drone seized by China, Pentagon says. https://www.cbsnews.com/news/china-seizes-us-underwater-drone-pentagon/, 2016.

[14] DS-USB-1608FS-Plus. Technical report, Measurement Computing, 2017.

[15] Promode R. Bandyopadhyay. Highly maneuverable biorobotic underwater vehicles. In *Springer Handbook of Ocean Engineering*, pages 281–300. 2016.

[16] J. Bellingham. Autonomous Underwater Vehicles (AUVs). In *Encyclopedia of Ocean Sciences*, pages 212–216. 2001.

[17] Brian Borowski, Alexander Sutin, Heui-Seol Roh, and Barry Bunin. Passive acoustic threat detection in estuarine environments. *International Society for Optics and Photonics*, 6945(Optics and Photonics in Global Homeland Security IV), 2008.

[18] A. M. Bradley, M. D. Feezor, H. Singh, and F. Yates Sorrell. Power systems for autonomous underwater vehicles. *Oceanic Engineering, IEEE Journal of*, 26(4):526–538, 2001.

[19] Andrew S. Brierley, Paul G. Fernandes, Mark A. Brandon, Frederick Armstrong, Nicholas W. Millard, Steven D. McPhail, Peter Stevenson, Miles Pebody, James Perrett, Mark Squires, Douglas G. Bone, and Gwyn Griffiths. Antarctic Krill Under Sea Ice: Elevated Abundance in a Narrow Band Just South of Ice Edge. *Science Magazine*, 295(8 March):1890–1892, 2002.

[20] Kevin Brinkmann and Jörg Hurka. Broadband Passive Sonar Tracking. *GI Jahrestagung*, pages 812–817, 2009.

[21] Mario P. Brito and Gwyn Griffiths. Autonomy: Risk assessment. In *Springer Handbook of Ocean Engineering*, pages 527–544. 2016.

[22] John S. Canning. A Definitive Work on Factors Impacting the Arming of Unmanned Vehicles. Technical Report May, Naval Surface Warfare Center, Dahlgren, 2005.

[23] Chris Lo. Persistent littoral surveillance: automated coast guards. `https://www.naval-technology.com/features/featurenavy-persistent-littoral-surveillance-auvs-uuvs/`, 2012.

[24] Kil Woo Chung, Alexander Sutin, Alexander Sedunov, and Michael Bruno. DEMON acoustic ship signature measurements in an urban harbor. *Advances in Acoustics and Vibration*, 2011(i), 2011.

[25] Bryan Clark. Game Changers – Undersea Warfare. Technical report, Center for Strategic and Budgetary Assessments, 2015.

[26] Michael Corinthios. Energy and Power Spectral Densities. In *Signals, Systems, Transforms, and Digital Signal Processing with MATLAB*, chapter 12, pages 825–863. CRC Press, 2009.

[27] Denise Crimmins and Justin Manley. What are auvs, and why do we use them? `https://oceanexplorer.noaa.gov/explorations/08auvfest/background/auvs/auvs.html`, 2008.

[28] J. Cuschieri and F. Debiesme. Characterizing the Sources of Noise and Vibration on a Small Autonomous Submersible. *International Congress and Exhibition on Noise Control Engineering*, (August):1–6, 2000.

[29] J.M. Cuschieri, M. Dhanak, and D. Vendittis. AUV Self Noise Control and Acoustic Signature Meaurements. Technical report, Department of Ocean Engineering, Florida Atlantic University, Boca Raton, 1998.

[30] DARPA. Special Notice DARPA-SN-16-11 1: Open Ocean Counter Unmanned Underwater Vehicle (OOCUUV) Study. Technical report, 2016.

[31] Ross L. Dawe. Detection Threshold Modelling Explained. pages 1–76, 1997.

[32] N. N. De Moura, J. M. De Seixas, and Ricardo Ramos. Passive Sonar Signal Detection and Classification Based on Independent Component Analysis. *Sonar Systems*, pages 93–103, 2011.

[33] Dan E. Dudgeon and Richard T. Lacoss. An Overview of Automatic Target Recognition. *The Lincoln Laboratory Journal*, 6(1):3–10, 1993.

[34] J. Dzielski, M. DeLorme, A. Sedunov, P. Sammut, and M. Tsionskiy. Guidance of an unmanned underwater vehicle using a passive acoustic threat detection system. *Waterside Security Conference (WSS), 2010 International*, pages 1–4, 2010.

[35] Megan Eckstein. Navy: Future Undersea Warfare Will Have Longer Reach, Operate With Network of Unmanned Vehicles. `https://news.usni.org/2016/03/24/navy-future-undersea-warfare-will-have-longer-reach-operate-with/network-of-unmanned-vehicles`, 2016.

[36] Megan Eckstein. DARPA, BAE Systems Developing Small Unmanned Underwater Vehicles to Hunt Enemy Submarines. `https://news.usni.org/2017/07/18/darpa-bae-systems-developing-small-uuv-to-conduct-active-sonar/sub-hunting-on-behalf-of-us-navy-subs`, 2017.

[37] Joshua Edwards and Dennis Gallagher. Mine and Undersea Warfare for the Future, 2014.

[38] Frank Ehlers. Cooperative Vehicle Target Tracking. In *Springer Handbook of Ocean Engineering*, pages 499–515. 2016.

[39] Donald Eickstedt and Michael Benjamin. Cooperative Target Tracking in a Distributed Autonomous Sensor Network. In *OCEANS 2006*, pages 1–6. IEEE, sep 2006.

[40] Donald P Eickstedt. *Adaptive Sampling in Autonomous Marine Sensor Networks*. PhD thesis, Massachusetts Institute of Technology, Woods Hole Oceanographic Institute, 2006.

[41] Donald P. Eickstedt, Michael R. Benjamin, Henrik Schmidt, and John J. Leonard. Adaptive control of heterogeneous marine sensor platforms in an autonomous sensor network. *IEEE International Conference on Intelligent Robots and Systems*, pages 5514–5521, 2006.

[42] Criag Fields, Ralph Semmel, and James Shields. DSB Task Force Report on Next-Generation Unmanned Undersea Systems. Technical report, Defense Science Board, Washington, DC, 2016.

[43] L. Fillinger, A.J. Hunter, M. Zampolli, and M.C. Clarijs. Passive acoustic detection of closed-circuit underwater breathing apparatus in an operational port environment. *The Journal of the Acoustical Society of America*, 132(10):700671121–14800503, 2012.

[44] Laurent Fillinger, Pascal De Theije, Mario Zampolli, Alexander Sutin, Hady Salloum, Nikolay Sedunov, and Alexander Sedunov. Towards a passive acoustic underwater system for protecting harbours against intruders. *2010 International Waterside Security Conference, WSS 2010*, 2010.

[45] Sydney J. Freedberg. Underwater Bloodhounds: DARPA's Robot Subs. https://breakingdefense.com/2017/07/underwater-bloodhounds-darpas-robot-subs/, 2017.

[46] Lee Freitag, Matthew Grund, Chris Chris Von Alt, Roger Stokey, and Thomas Austin. A Shallow Water Acoustic Network for Mine Countermeasures Operations with Autonomous Underwater Vehicles. *Underwater Defense Technology (UDT)*, pages 1–6, 2005.

[47] David Fries and William Kirkwood. Non-acoustic sensors. In *Springer Handbook of Ocean Engineering*, pages 423–439. 2016.

[48] Franz-Stefan Gady. Confirmed: US Navy Launches Underwater Drone From Sub. https://thediplomat.com/2015/07/confirmed-us-navy-launches-underwater-drone-from-sub/, 2015.

[49] John Gebbie, Martin Siderius, and J. S. Allen. Passive Acoustic Array Harbor Security Applications. *Marine Technology Society Journal*, 45(3):103–110, 2011.

[50] John Gebbie, Martin Siderius, and John S. Allen III. Aspect-dependent radiated noise analysis of an underway autonomous underwater vehicle. *Journal of Acoustical Society of America*, 2012.

[51] John Gebbie, Martin Siderius, Reid Mccargar, John S Allen III, and Grant Pusey. Localization of a noisy broadband surface target using time differences of multipath arrivals. *Journal of Acoustical Society of America*, 2013.

[52] John Gebbie, Martin Siderius, Peter L. Nielsen, and James Miller. Passive localization of noise-producing targets using a compact volumetric array. *Journal of Acoustical Society of America*, 2014.

[53] Gwyn Griffiths, Peter Enoch, and Nicholas W. Millard. On the radiated noise of the Autosub autonomous underwater vehicle. *ICES Journal of Marine Science – ICES Journal of Marine Science*, 58(58):1195–1200, 2001.

[54] Matthew Grund, Lee Freitag, James Preisig, and Keenan Ball. The PLUSNet underwater communications system: Acoustic telemetry for Undersea Surveillance. *Oceans 2006*, 2006.

[55] Ricardo Gutierrez-Osuna. Introduction to Speech Processing. Technical report, Perception, Sensing, Instrumentation Lab, Texas A&M University.

[56] Per Espen Hagen, Oyvind Hegrenes, Bjorn Jalving, Oiyvind Midtgaard, Martin Wiig, and Ove Ken Hagen. Making AUVs truly autonomous. In *OCEANS 2007*, pages 1–4. IEEE, 2007.

[57] Michael J. Hamilton, Stephanie Kemna, and David Hughes. Antisubmarine warfare applications for autonomous underwater vehicles: The GLINT09 sea trial results. *Journal of Field Robotics*, 27(6):890–902, nov 2010.

[58] Oistein Hasvold, Nils J. Storkersen, Sissel Forseth, and Torleif Lian. Power sources for autonomous underwater vehicles. *Journal of Power Sources*, 162(2 SPEC. ISS.):935–942, 2006.

[59] Jason D. Holmes, William M. Carey, and James F. Lynch. Results from the Nantucket Sound autonomous underwater vehicle towed hydrophone array experiment. *The Journal of the Acoustical Society of America*, 120, 2006.

[60] Jason D. Holmes, William M. Carey, and James F. Lynch. An overview of unmanned underwater vehicle noise in the low to mid frequencies bands. *Acoustical Society of America*, 9, 2010.

[61] Paul Hornsby. Autonomous Underwater Vehicles Capability and Trends. Technical report, Royal Australian Navy, 2016.

[62] John Howard. Fixed SONAR Systems the History and Future of the Underwater Silent Sentinel. *The Submarine Review*, pages 1–12, 2011.

[63] Stephanie Kemna, Michael J. Hamilton, David T. Hughes, and Kevin D. LePage. Adaptive autonomous underwater vehicles for littoral surveillance. *Intelligent Service Robotics*, 4(4):245–258, 2011.

[64] James C. Kinsey, Ryan Eustice, and Louis L. Whitcomb. A Survey of Underwater Vehicle Navigation: Recent Advances and New Challenges. *IFAC Conference of Manoeuvring and Control of Marine Craft (MCMC 2006)*, 88:1–12, 2006.

[65] John J. Leonard and Alexander Bahr. Autonomous underwater vehicle navigation. In *Springer Handbook of Ocean Engineering*, pages 341–357. 2016.

[66] Naomi Ehrich Leonard. Cooperative vehicle environmental monitoring. In *Springer Handbook of Ocean Engineering*, pages 441–458. 2016.

[67] Pierre F.J. Lermusiaux, Tapovan Lolla, Patrick J. Haley, Konuralp Yigit, Mattheus P. Ueckermann, Thomas Sondergaard, and Wayne G. Leslie. Science of autonomy: Time-optimal path planning and adaptive sampling for swarms of ocean vehicles. In *Springer Handbook of Ocean Engineering*, pages 481–497. 2016.

[68] Te-Chih Liu and Henrik Schmidt. AUV-Based Seabed Target Detection and Tracking. *IEEE*, 2002.

[69] T. Lolla, P.J. Haley, and P.F.J. Lermusiaux. Path planning in multi-scale ocean flows: Coordination and dynamic obstacles. *Ocean Modelling*, 94:46–66, 2015.

[70] Ray Mabus. Autonomous Undersea Vehicle Requirement for 2025. Technical report, U.S. Navy, Washington, DC, 2016.

[71] Darren K. Maczka, Davide Spinello, Daniel J. Stilwell, Aditya S. Gadre, and Wayne L. Neu. Coordinated tracking of an acoustic signal by a team of autonomous underwater vehicles. *AUVSI Unmanned Systems North America Conference 2009*, 2:1016–1033, 2009.

[72] Robert C. Manke and Raymond J. Christian. Asymmetry in Maritime Access and Undersea Anti-Access/Area-Denial. Technical Report August, Office of the Director of Undersea Warfare, 2007.

[73] Adam Mara. Bluefin Sandshark. Technical report, General Dynamics - Bluefin Robotics, Quincy, 2018.

[74] Matthew Ritchey. Unmanned Undersea Vehicles: An Asymmetric Tool for Sea Denial. Master's thesis, Naval War College, 2008.

[75] Alejandro Mendez, Teresa J. Leo, and Miguel A. Herreros. Current state of technology of fuel cell power systems for autonomous underwater vehicles. *Energies*, 7(7):4676–4693, 2014.

[76] George L. Ogden, Lisa M. Zurk, Mark E. Jones, and Mary E. Peterson. Extraction of small boat harmonic signatures from passive sonar. *The Journal of the Acoustical Society of America*, 129(107), 2011.

[77] Alan V. Oppenheim and George C. Verghese. Power Spectral Density. *MIT OpenCourseWare: 6.011 Introduction to Communication, Control, and Signal Processing*, pages 183–195, 2010.

[78] Alan V. Oppenheim, Alan S. Willsky, and S. Hamid Nawab. *Signals and Systems*. Prentice Hall, Upper Saddle River, 1997.

[79] Stephanie Petillo, Henrik Schmidt, and Arjuna Balasuriya. Constructing a Distributed AUV Network for Underwater Plume-Tracking Operations. *International Journal of Distributed Sensor Networks*, 2012.

[80] Mark Pomerleau. DOD plans to invest $600M in unmanned underwater vehicles. `https://defensesystems.com/articles/2016/02/04/dod-navy-uuv-investments.aspx`, 2016.

[81] H. Rice, S. Kelmenson, and L. Mendelsohn. Geophysical navigation technologies and applications. *PLANS 2004. Position Location and Navigation Symposium (IEEE Cat. No.04CH37556)*, pages 618–624.

[82] M. Samseer. US Navy uses undersea wireless technology to recharge UUVs. `https://www.naval-technology.com/uncategorised/newsus-navy-uses-undersea-wireless-technology-to-recharge-uuvs/4657347/`, 2015.

[83] Henrik Schmidt, Michael R Benjamin, Stephanie M Petillo, and Raymond Lum. Nested autonomy for distributed ocean sensing. In *Springer Handbook of Ocean Engineering*, pages 459–479. 2016.

[84] Science and Technology Organization Centre for Maritime Research and Experimentation Cooperative. Cooperative Antisubmarine Warfare. Technical report, CMRE, La Spezia.

[85] Mae L. Seto. *Marine Robot Autonomy*. Springer Science & Business Media, 2012.

[86] Martin Siderius and John Gebbie. Ocean Ambient Noise Studies for Improved Sonar Processing. Technical report, Electrical and Computer Engineering, Portland State University, 2012.

[87] Erik Sofge. MIT Submarine Is Most Autonomous Robot Ocean Researcher Yet. `https://www.popularmechanics.com/technology/robots/a12502/4285189/`, 2009.

[88] Milica Stojanovic and Pierre-Philippe J. Beaujean. Acoustic Communication. *Springer Handbook of Ocean Engineering*, pages 359–386, 2016.

[89] Milica Stojanovic and James Preisig. Underwater acoustic communication channels: Propagation models and statistical characterization. *Communications Magazine, IEEE*, 47(1):84–89, 2009.

[90] Dan Suchman and Thomas Meurling. Integrated underwater intruder detection system. In *2010 International WaterSide Security Conference*, pages 1–8. IEEE, 2010.

[91] Shelby Sullivan. Mobile Offboard Command, Control and Attack (MOCCA). `https://www.darpa.mil/program/mobile-offboard-clandestine-communications-and-approach`.

[92] Harry L Van Trees. Characterization of Space-time Processes. In *Optimum Array Processing: Part IV of Detection, Estimation, and Modulation Theory*, chapter 5. John Wiley & Sons, Inc., 2002.

[93] Harry L. Van Trees. Optimum Waveform Estimation. In *Optimum Array Processing: Part IV of Detection, Estimation, and Modulation Theory*, chapter 6. John Wiley & Sons, Inc., 2002.

[94] Harry Van Trees. Arrays and Spatial Filters. In *Optimum Array Processing: Part IV of Detection, Estimation, and Modulation Theory*, chapter 2, pages 17–89. John Wiley & Sons, Inc., 2002.

[95] Michael S. Triantafyllou and Franz S. Hover. Maneuvering and Control of Marine Vehicles. *Massachusetts Institute of Technology*, pages 105–110, 2003.

[96] Edward Tucholski. Detection Theory. In *Underwater Acoustics and Sonar SP411 Handouts and Notes*, chapter 15. Annapolis, 2006.

[97] U.S. Navy. The Navy Unmanned Undersea Vehicle (UUV) Master Plan. 2004.

[98] Rebecca Willet. Receiver Operating Characteristic (ROC) Curve. In *ECE 830*, chapter 8, pages 1–21. University of Wisconsin-Madison, Madison, 2014.

[99] Russell B. Wynn, Veerle A.I. Huvenne, Timothy P. Le Bas, Bramley J. Murton, Douglas P. Connelly, Brian J. Bett, Henry A. Ruhl, Kirsty J. Morris, Jeffrey Peakall, Daniel R. Parsons, Esther J. Sumner, Stephen E. Darby, Robert M. Dorrell, and James E. Hunt. Autonomous Underwater Vehicles (AUVs): Their past, present and future contributions to the advancement of marine geoscience. *Marine Geology*, 352:451–468, 2014.

[100] Xuri Yu, Tommy Dickey, James Bellingham, Derek Manov, and Knut Streitlien. The application of autonomous underwater vehicles for interdisciplinary measurements in Massachusetts and Cape Cod Bays. *Continental Shelf Research*, 22:2225–2245, 2002.

[101] Z. Y. Zhang. Diver Detection Sonars and Target Strength: Review and Discussions. *14th International Congress on Sound & Vibration*, pages 1–8, 2007.

[102] Richard Zimmerman, Gerald L. D'Spain, and C. David Chadwell. Decreasing the radiated acoustic and vibration noise of a mid-size AUV. *IEEE Journal of Oceanic Engineering*, 30(1):179–187, 2005.